SAND2018-10095C

2018-01-1794 Published 10 Sep 2018

Bowl Geometry Effects on Turbulent Flow Structure in a Direct Injection Diesel Engine

Stephen Busch and Kan Zha Sandia National Laboratories

Federico Perini University of Wisconsin-Madison

Rolf Reitz University of Wisconsin

Eric Kurtz Ford Motor Company

Alok Warey General Motors Global R & D

Richard Peterson General Motors LLC

Citation: Busch, S., Zha, K., Perini, F., Reitz, R. et al., "Bowl Geometry Effects on Turbulent Flow Structure in a Direct Injection Diesel Engine," SAE Technical Paper 2018-01-1794, 2018, doi:10.4271/2018-01-1794.

Abstract

Diesel piston bowl geometry can affect turbulent mixing and therefore it impacts heat-release rates, thermal efficiency, and soot emissions. The focus of this work is on the effects of bowl geometry and injection timing on turbulent flow structure. This computational study compares engine behavior with two pistons representing competing approaches to combustion chamber design: a conventional, re-entrant piston bowl and a stepped-lip piston bowl. Three-dimensional computational fluid dynamics (CFD) simulations are performed for a part-load, conventional diesel combustion operating point with a pilot-main injection strategy under non-combusting conditions. Two injection timings are simulated based on experimental findings: an injection timing for which the stepped-lip piston enables significant efficiency and emissions benefits, and an injection timing with diminished benefits compared to the conventional, re-entrant piston.

While the flow structure in the conventional, re-entrant combustion chamber is dominated by a single toroidal vortex, the turbulent flow evolution in the stepped-lip combustion chamber depends more strongly on main injection timing. For the injection timing at which faster mixing controlled heat release and reduced soot emissions have been observed experimentally, the simulation predicts the formation of two additional recirculation zones created by interactions with the stepped-lip. Analysis of the CFD results reveals the mechanisms responsible for these recirculating flow structures. Vertical convection of outward radial momentum drives the formation of the recirculation zone in the squish region, while adverse pressure gradients drive flow inward near the cylinder head, thereby contributing to the formation of the second recirculation zone above the step. Bulk gas density is higher for the near-TDC injection timing than for the later injection timing. This leads to increased air entrainment into the sprays and slower spray velocities, so the sprays take longer to interact with the step, and beneficial recirculating flow structures are not obseved.

Introduction

Combustion chamber geometry, together with swirl level and injector nozzle parameters, are the primary design parameters that influence the pollutant emissions behavior and thermal efficiency of a diesel combustion system [1, 2]. This work is concerned with two competing approaches to combustion chamber designs for light- and medium-duty engines: conventional, re-entrant piston bowls, and stepped- or chamfered-lip piston bowls. The reader is referred to [3] for a more detailed summary of stepped-lip designs. Recent work to compare engine behavior with a stepped-lip and a conventional piston has demonstrated that for a range of injection timings shortly after top dead center (TDC), the use of the stepped-lip piston results in faster mixing controlled heat release. Faster heat release rates more closely resemble ideal, constant volume heat release, and therefore result in higher thermal efficiencies [4]. The focus of this work is on the in-cylinder processes that influence turbulent flow structure and mixing.

For combustion chambers with conventional, re-entrant piston bowls, in-cylinder flow before fuel injection is dominated by squish-swirl interactions [5, 6]. The competition between squish flow and centrifugal force, which increases as squish flow does work on the swirling flow to increase its angular velocity, yields a vertical-plane flow structure: a toroidal vortex carrying fuel-rich mixture in the bowl. Fuel injection has a similar impact on the flow as interactions between radial momentum delivered by the jets and the

 Sandia National Laboratories is a multimission laboratory managed and operated by National Technology & Engineering Solutions of Sandia, LLC, a wholly owned subsidiary of Honeywell International Inc., for the U.S. Department of Energy's National Nuclear Security Administration under contract DE-NA0003525.

centrifugal forces associated with the swirling flow enhance existing toroidal vortices. In some cases, an upper toroidal vortex may form in the oxygen-rich mixture above the pip. The interface between the two toroidal vortices is associated with flow distortion and thus promotes turbulence generation and fuel-air mixing [6]. Additionally, the radial momentum of the sprays can perform work on the swirling flow to displace regions of high angular momentum and store energy in the form of mean flow rotation. This rotational energy can be released later in the cycle as turbulence [6]. The redistribution of angular momentum can lead to tangential velocity gradients that promote late-cycle turbulence generation [7]. Finally, the squish flow changes direction as the piston begins to move downward. This is called "reverse squish flow" and is associated with large velocity gradients above the piston face and near the bowl rim, and separation of the flow exiting the bowl near the bowl lip. These phenomena serve to generate turbulence during the reverse squish event, but this turbulence appears to dissipate within approximately 20 crank angle degrees (CAD) of TDC [8]. More detail about turbulent flows in engines with conventional, re-entrant piston bowls is given in [8].

Stepped-lip bowls are often associated with beneficial changes in turbulent flow structure and mixing behavior, but the mechanisms responsible for these changes are not well documented. Air utilization may improve through fuel splitting at the step, thereby decreasing soot emissions and potentially improving efficiency. Dolak et al. suggest that two injections combined with a stepped-lip geometry can improve air utilization and result in two spatially separated combustion events [9]. Styron et al. compare a conventional, re-entrant piston bowl with a stepped-lip bowl; their CFD simulation results suggest that the stepped-lip piston produces a more even mixture distribution above the squish region [2]. Additionally, dual-vortex flow structures that result from spray-wall interactions are frequently cited as a means of air utilization enhancement and reduced soot emissions [1, 10, 11, 12]. Comparisons between stepped-lip and conventional, re-entrant combustion chambers often reveal higher mixing controlled heat-release rates with the stepped-lip piston [10, 11, 13]. Kurtz et al. theorize that improved air utilization in the squish region may be responsible for higher mixing-controlled heat-release rates [13]. A related possibility is that the dual vortex flow structures enhance turbulent fuel-air mixing rates [11] and thereby improve thermal efficiency [4].

Recent experimental studies with a conventional, re-entrant piston and a stepped-lip piston indicate that for a part-load operating point, benefits in mixing controlled heat-release rates that result from the use of the stepped-lip bowl are obtained for a finite range of main injection timings [4]. Similarly, reductions in smoke emissions (reported in [3]) may only be achieved with the stepped-lip piston for a limited range of injection timings. The efficiency, combustion phasing, and smoke emissions data are summarized in Figure 1. For this part-load operating point, the efficiency advantages of the stepped-lip piston are most significant for main injections starting after TDC. The advantages in mixing-controlled heat release rates and smoke emissions are greatest for main injection timings after 5 CAD after TDC. The combined advantages of the stepped-lip piston appear to reach their maximum for

FIGURE 1 Closed portion thermal efficiency (top), combustion phasing (middle), and smoke emissions (bottom) for the conventional (blue open symbols) and stepped-lip (red closed symbols) pistons for a conventional, part-load operating point with a pilot-main injection strategy. See [3, 4] for descriptions of the experimental conditions.

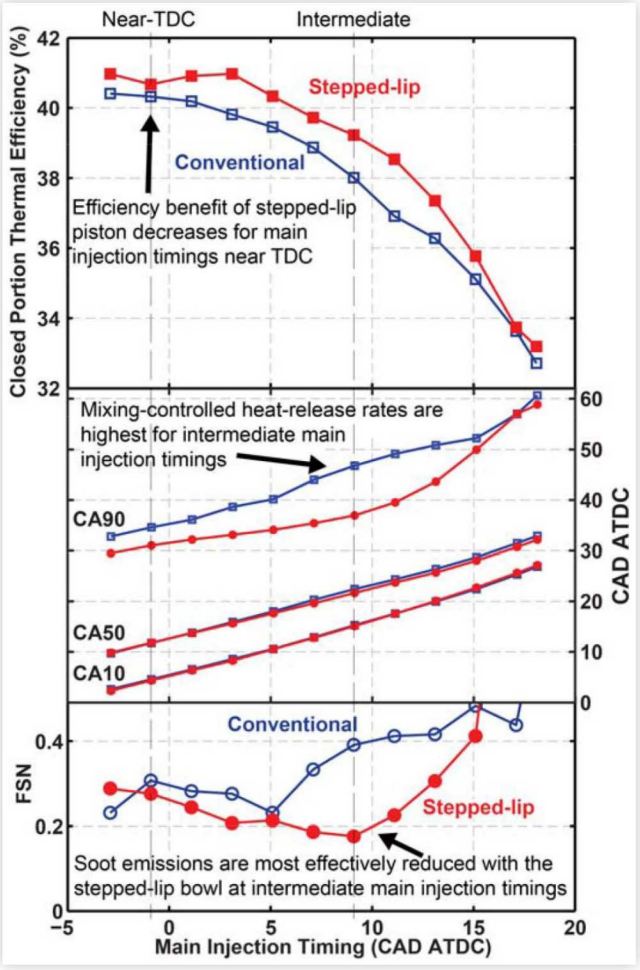

intermediate injection timings (between approximately 5 and 13 CAD after TDC), whereas one or all of the advantages are diminished as injection timing is advanced or retarded from this intermediate timing.

Optical characterization of turbulent flow with a stepped-lip bowl provides evidence of long-lived, recirculating flow structures in the squish region that coincide with enhanced heat-release rates for optimal injection timings [3]. These recirculating flow structures are not observed with the conventional, re-entrant piston bowl and must therefore be produced through interactions with the stepped-lip geometry. However, cause-effect relationships between injection timing; geometrical features of stepped-lip bowls; turbulent flow-structure evolution; and turbulent mixing, have not yet been documented.

The objectives of this computational comparison of a conventional, re-entrant bowl and a stepped-lip bowl are threefold:

1. Compare the evolution of turbulent flow topology in the conventional and in the stepped-lip combustion

chambers for a representative intermediate injection timing (start of main injection: 9.1 CAD after TDC).

2. Describe the mechanism by which the stepped-lip bowl fosters flow structures that result in faster turbulent fuel-air mixing than with the conventional bowl for intermediate injection timings.
3. Explain why the advantages of the stepped-lip piston are diminished at a representative injection timing near TDC (start of main injection: 0.9 CAD before TDC).

To this end, multi-cycle CFD simulations are performed using a model of a small-bore optical diesel engine with both a re-entrant piston and a stepped-lip piston. This study focuses on a part-load, conventional diesel operating point with a pilot-main injection strategy under non-combusting conditions for two main injection timings. Analyses of these results in the context of the radial momentum equation provide new understanding of turbulent flow evolution in the stepped-lip combustion chamber, and provide insights into the injection timing sensitivity of the emissions and efficiency benefits associated with the stepped-lip combustion chamber.

CFD Simulations

The FRESCO CFD simulation platform is used to solve the Reynolds-averaged Navier-Stokes (RANS) equations on a full engine mesh. More details about FRESCO are given in [14]. Turbulence is modeled using a generalized re-normalization group (RNG) turbulence closure model that has been validated with engine flows, as well as for impinging and reacting jets [14, 15]. Fuel injection and spray phenomena are modeled with a Lagrangian-Particle/Eulerian-Fluid approach. Table 1 is a summary of the sub-models used to simulate turbulence and sprays. The spray sub-model parameters have been simultaneously optimized with a multi-objective genetic algorithm based on Engine Combustion Network (ECN) spray A data [16, 17]. No further tuning has been performed for the current study, as comparisons with experimental liquid and fuel vapor data show very good agreement (see, for example, [18]).

TABLE 1 CFD sub-models for turbulence and spray

Fluid dynamical phenomenon	Modeling approach
Turbulence	Generalized re-normalization group (GRNG) k-ε [15]
Injection	Blob model with dynamic blob allocation [17]
Spray angle	Semi-empirical correlation [19]
Spray breakup	Hybrid Kelvin-Helmholtz / Rayleigh-Taylor (KH-RT) [20]
Droplet drag	Analytical with Mach number and droplet distortion effects [17]
Droplet collision	Deterministic impact; bounce, coalescence, reflexive separation, and stretching separation [21]; dynamic radius of influence [17]
Evaporation	Discrete multicomponent fuel model [22]
Near-nozzle flow	Sub-grid scale, unsteady gas-jet model [17]

TABLE 2 Engine and fuel injector geometry data

Bore	82.0 mm
Stroke	90.4 mm
Connecting rod length	166.7 mm
Squish height	1.36 mm
Geometric compression ratio	15.8: 1
Injector nozzle holes x diameter	7 x 139 μm
Nozzle hole conicity (k_s)	1.5
Injector included angle	149°

The Sandia small-bore diesel engine, which is built with a GM 1.9 L cylinder head, is modeled in this study. The full engine geometry includes the intake and exhaust surge tanks, the intake and exhaust runners, the swirl plates in the intake runners, the intake and exhaust ports, the cylinder head, and the optical pistons. The full engine geometric data are available on the ECN website [23], and are briefly summarized in Table 2. An unstructured, body-fitted, hexahedral mesh is generated for the full engine and for each piston geometry (see [24] for more details of the mesh geometry). The unstructured meshes are comprised of approximately 705,000 and 724,000 cells at bottom dead center for the conventional and stepped-lip piston bowls, respectively. The meshes are depicted in Figure 2.

Details of the 7-hole injector used in this study are also given in Table 2. Spray targeting in the simulation matches the spray targeting used in corresponding optical and thermodynamic engine experiments, and has been adjusted for each piston by varying the axial position of the nozzle holes (see Table 3). The specific spray targeting data used in this study are available on the ECN website, as well as measured injection rate data for the baseline cases [23].

Multiple consecutive cycles are simulated as follows to reach a compromise between sensitivity to initial conditions and total computational time. The simulation is initialized at the time of exhaust valve opening of cycle 0. The in-cylinder flow field is represented as solid body rotation with a small residual swirl ratio (R_s, the ratio of flow rotational speed to engine speed, is taken to be 0.05; see [25] for a more detailed explanation of R_s). Turbulence levels, density, pressure, temperature, and composition are homogeneous and set for each of three regions: the cylinder; the intake ports, runners, and surge tank; and the exhaust ports, runners, and surge tank. Cycle 1 is simulated in its entirety but without fuel injection. Results of previous investigations indicate that after this cycle, the most energetic features of in-cylinder flow are converged and agree well with particle image velocimetry data [26]. Simulation continues through all of cycle 2, during which the fuel injection is simulated; all results shown in this work are taken from cycle 2. The total simulation time is approximately 35 hours for each case.

Engine operation parameters and boundary conditions are given in Table 3 and represent corresponding experimental conditions for which experimental data are available [3, 4]. This is a part-load, conventional diesel combustion operating point with a pilot-main injection strategy. The intake charge

FIGURE 2 Full-engine CFD mesh used in this study. Cutaway views are shown to depict each piston bowl. The large intake and exhaust plenums are accurate representations of the single-cylinder research engine setup.

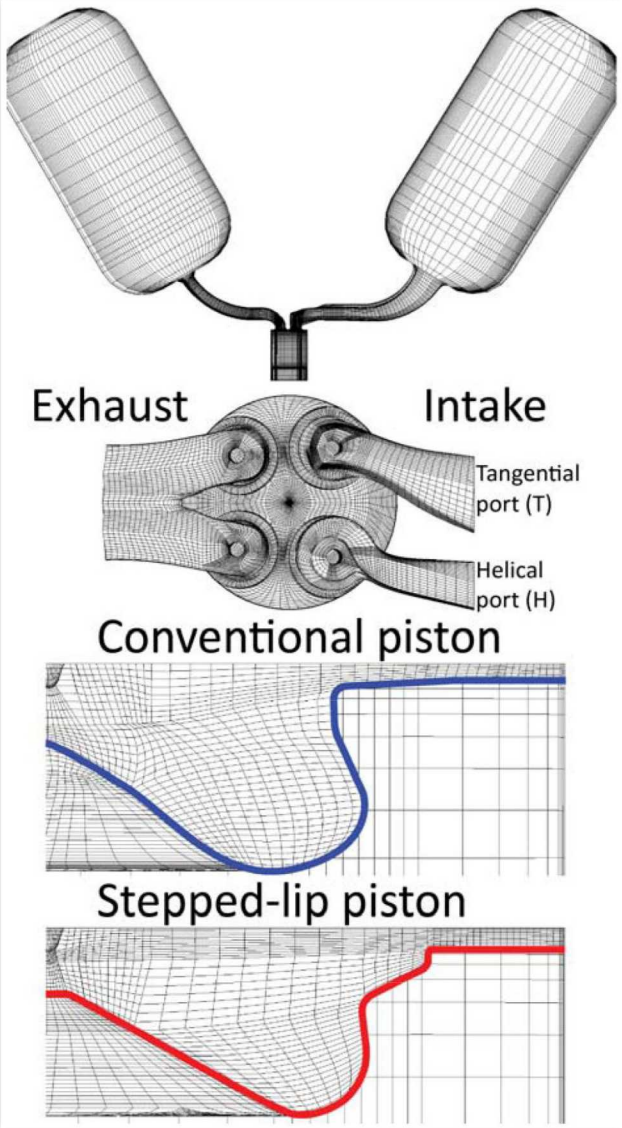

is comprised of 100% N_2 to facilitate comparison with optical engine data (see [18]). Simulated gas flow rates are typically within 5-7% of the flow rates in the experiments; experimental uncertainties in the pressure boundary conditions are believed to be a limiting factor. The surface temperatures given in Table 3 are held constant; they have been inferred from the coolant temperature and from previous simulation experience. The pilot-main dwell is held constant, and the injection schedule is block shifted to simulate two different injection-timing cases. The intermediate start of main injection (SOI_{main}) of 9.1 CAD ATDC results in significant efficiency and soot emissions benefits for the stepped-lip piston, whereas these benefits are diminished for the near-TDC injection timing or the latest injection timing (see Figure 1).

Injection rate profiles are measured with a hydraulic injection rate meter based on the injector solenoid energizing

TABLE 3 Engine operating point and simulation boundary conditions. Note the naming convention for the two injection timings.

Engine speed	1500 rpm
Intake pressure	151 kPa
Intake temperature	329 K
Coolant temperature	363 K
Piston surface temperature	440 K
Liner temperature	430 K
Head temperature	440 K
Intake valve temperature	370 K
Exhaust valve temperature	400 K
Intake port temperature	329 K
Exhaust port temperature	410 K
Exhaust pressure (constant)	145.7 kPa
Intake charge composition	100 vol% N_2 (non-combusting)
Swirl ratio (Ricardo)	2.2 (both intake swirl plates open)
Fuel	58 vol% 2,2,4,4,6,8,8-heptamethylnonane, 42 vol% n-hexadecane
$IMEP_g$ (engine experiments)	9 bar
Injection pressure (baseline)	800 bar
Pilot-main hydraulic dwell	11.5 CAD
Start of main injection (SOI_{main})	**Near-TDC:** 0.9 CAD BTDC, **Intermediate:** 9.1 CAD ATDC
Axial distance between the nozzle holes and the fire deck	Conventional: 1.07 mm, Stepped-lip: 1.35 mm

FIGURE 3 Injection rate profiles for the near-TDC and intermediate main injection timings.

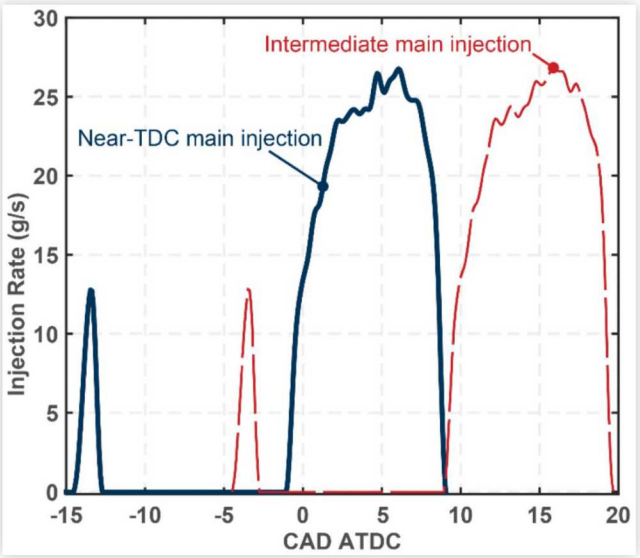

times used in engine testing for each main injection timing and for both piston geometries. The injection rates for the near-TDC and intermediate main injection events are shown in Figure 3. For details of the experimental setup used to measure injection rates, please see [27].

Results and Discussion

Bowl Geometry Impact on Fuel Splitting and Turbulent Flow Structure

Because efficiency and soot emissions are most sensitive to bowl geometry at the intermediate main injection timing (see Figure 1), this injection timing is studied to understand bowl geometry's influence on fuel splitting, turbulent flow structure, and mixing.

Fuel splitting at the bowl rim is quantified by applying a level-set analysis technique to the CFD results. To this end, a level-set function is generated in the computational domain such that the zero level is the conical surface containing the spray axes. This conical surface remains stationary; it does not move with the piston. At each crank angle, the portion of fuel above this surface is computed; the resulting plot is shown in Figure 4. The pilot injection does not split evenly above and below the spray axes, which is why both curves in Figure 4 start at values higher than 0.5. The difference between the starting behavior of each curve are likely related to differences in in-cylinder flow and changes in air entrainment for the different injector positions (shown in Table 3). Because the spray axes are closer to the cylinder head with the conventional piston (see Table 3), more upward deflection may be expected due to the Coandă effect. During the main injection, most of the fuel in the cylinder is located above the spray axes. However, after approximately 15 CAD ATDC, fuel is more evenly split between the upper and lower regions with the conventional bowl. With the stepped-lip bowl, the portion of fuel located above the spray axes begins to increase after 12 CAD ATDC, and after 15 CAD ATDC, more fuel exists above the spray axes with the stepped-lip bowl than with the conventional bowl. In other words, with the stepped-lip bowl, most of the main injection remains in the upper portion of the combustion chamber, whereas fuel is split nearly equally between the upper and lower regions of the conventional combustion chamber.

There are two potential explanations for the behavior shown in Figure 4. The first is that injected fuel will naturally fill the available space in the combustion chamber. Because more volume is available in the upper portion of the stepped-lip piston bowl, a greater fraction of the injected fuel could exist above the spray axes than for the conventional bowl. Figure 5 shows the portion of the total cylinder volume that exists above the spray axes for each bowl geometry as a function of crank angle. The portion of the stepped-lip combustion chamber that exists above the spray axes reaches a maximum of approximately 60% near 20 CAD ATDC, and decreases at an increasing rate after this. Figure 4 shows that during the main injection, the portion of fuel located above the spray axes increases, and continues to increase above 60% after the end of the injection, when the differences in volume ratio are decreasing (shown in Figure 5). Furthermore, for the conventional bowl, the portion of the cylinder volume that exists above the spray axis increases more dramatically during the first 28 CAD of the expansion stroke. The volume ratio reaches a maximum value of nearly 57%. However, the portion

FIGURE 4 Portion of total in-cylinder fuel located above the spray axes as a function of crank angle for the intermediate main injection timing. A value of 0.5 represents even splitting above and below the spray axes.

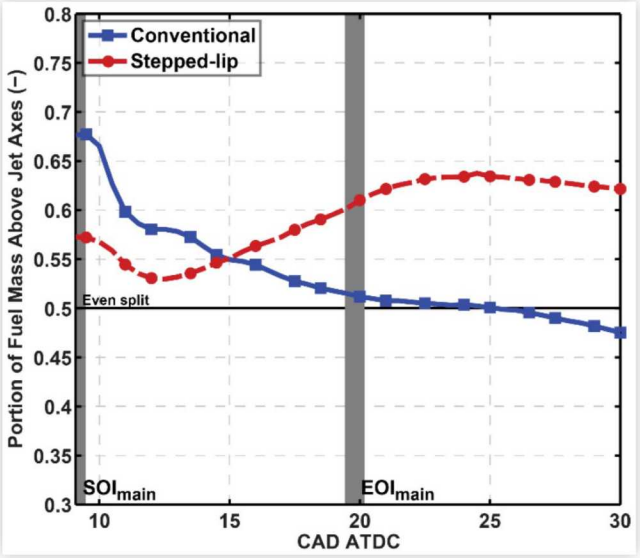

FIGURE 5 Fraction of cylinder volume located above the spray axes for each piston geometry as a function of crank angle. Cross sections of the volumes are depicted at the bottom right. The small difference after 30 CAD ATDC is because the vertical positions of the spray axes are different for each piston.

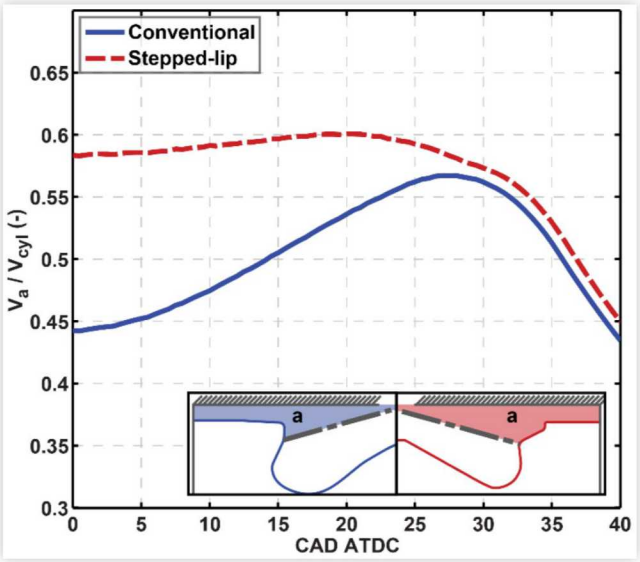

of the fuel above the spray axes decreases monotonically during and after the main injection. The volume ratio and the fuel mass ratio follow very different trends. Thus, this first mechanism of fuel filling the available space in the combustion chamber cannot explain the distribution of fuel within the cylinder.

The second potential mechanism responsible for the behavior shown in Figure 4 is that interactions between the

sprays, the combustion chamber geometry, and the in-cylinder flow field determine the fuel split ratio. The evolution of the fuel spray and vertical-plane velocity fields is depicted in Figure 6 for both piston geometries and for a single spray at various crank angles. The same spray is used for both the conventional (left column) and the stepped-lip (right column) piston bowls, but the stepped-lip images have been flipped to facilitate comparison, and all images have been horizontally compressed to fit in the column.

Although the simulated intake charge is 100% nitrogen, fuel-air equivalence ratios are computed from the simulated fuel concentration χ_{fuel} using the following equation [28]:

$$\phi = \frac{\chi_{fuel}}{1-\chi_{fuel}} \frac{24.5}{\chi_{O_2}} \quad (1)$$

χ_{O_2} is set to 19.7% to mimic experimental conditions [4].

The flow features that develop vary in relative significance and location for each spray, but what follows is a general description of the behavior observed throughout the cylinder.

At a crank angle of 14 CAD ATDC (top row of Figure 6), fuel vapor is just beginning to interact with the conventional bowl, but has not yet reached the stepped-lip bowl, which is larger in diameter. Experimental results indicate that high-temperature ignition of the main injection has occurred several CAD before this point in time. Differences in the simulated spray structure are observed in the spray heads, as stagnation at the conventional bowl rim causes the spray to spread outward, away from its axis. This interaction with the conventional bowl continues and by 16.5 CAD ATDC (second row of Figure 6), the spray has begun to split: a portion of it is deflected downward into the re-entrant bowl, and the upper spray continues to propagate outward into the squish region. Interactions with the stepped-lip bowl have also begun by 16.5 CAD ATDC, and they result in different vertical-plane flow fields than those with the conventional bowl. While the portions of the sprays that are deflected down into both bowls result in similar toroidal vortex flow patterns, the step surface and upper rim of the stepped-lip bowl impart a strong upward velocity to the upper portion of the propagating spray. With the conventional bowl, the vertical velocity components near the spray heads are considerably smaller, so that the upper portion of the spray continues to propagate rapidly outward above the conventional bowl.

The influx of fuel and momentum from the main injection ends shortly before 19.5 CAD ATDC (see Figure 3), but spray-wall interactions continue to evolve and play a role in establishing late-cycle flow patterns. As the piston moves downward during the main injection, an increasingly large portion of the spray does not interact with the conventional bowl rim, but propagates directly outward into the squish region. This continued delivery of outward momentum is evident in the relatively large fraction of the upper spray with a horizontal velocity component (third row, first column of Figure 6). The distribution of outward and upward momentum does not result in any well-organized or long-lived recirculation zones in the squish region above the conventional bowl. In contrast, the upper rim of the stepped-lip piston continues to deflect the upper portion of the spray upward, and at 19.5 CAD ATDC, this secondary spray has reached the cylinder head (third row, right column of Figure 6). The spray also continues its outward penetration, and a recirculating flow pattern begins to form in the outer portion of the squish region. Another portion of the secondary spray is redirected inward near the cylinder head. Together with the entrainment flow and outward spray

FIGURE 6 Vertical cross-section containing a spray axis showing fuel-air equivalence ratio and velocity fields projected onto the cutting plane for the intermediate injection timing. Velocity vectors are colored according to the magnitude of the projection of the velocity onto the cutting plane. The same spray is shown for each bowl geometry, but the images for the stepped-lip bowl have been mirrored to facilitate comparison. All images have been compressed horizontally to fit in the column. Yellow arrows have been added to indicate trends in spray propagation.

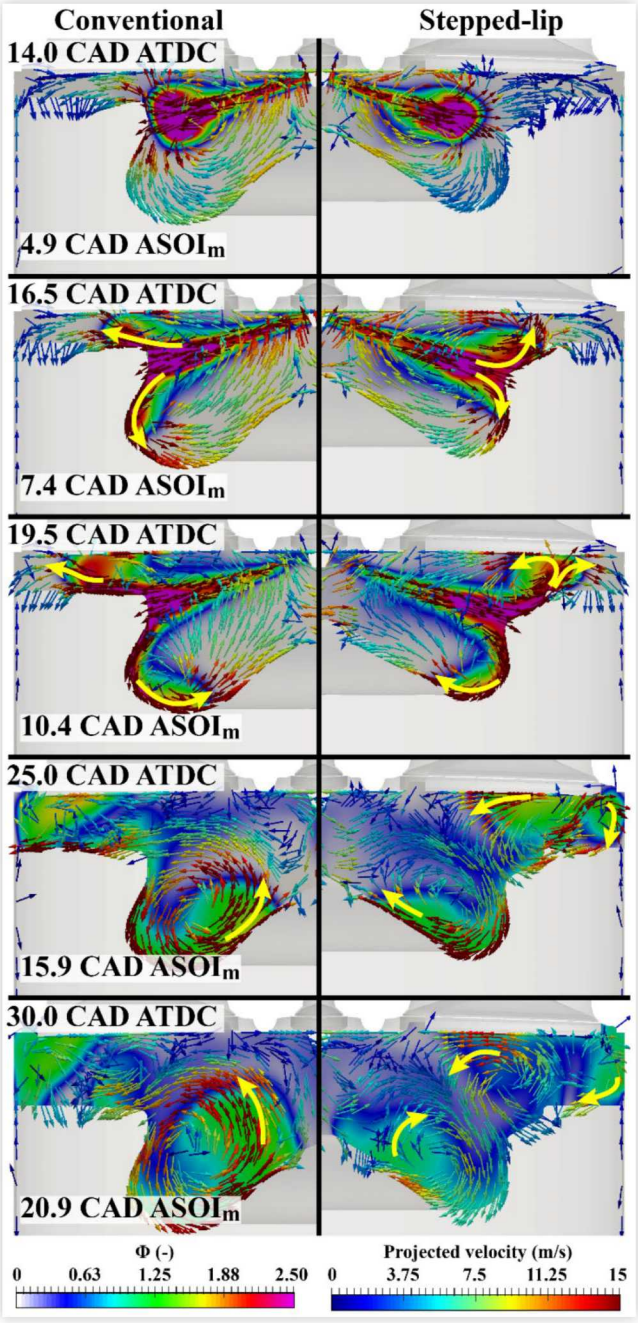

momentum, it forms yet another recirculation zone above the step.

At 25 CAD ATDC, the flow structure in the conventional, re-entrant combustion chamber is dominated by the toroidal bowl vortex, while outward flow continues in the squish region near the piston surface (fourth row, first column of Figure 6). A toroidal vortex also persists in the stepped-lip bowl, but the mixture contained in it remains in the lower portion of the bowl as the size and shape of the vortex are constrained (fourth row, second column of Figure 6). In the squish region above the stepped-lip bowl, two recirculation zones are observed: one in the outer portion of the squish region, and one located above the upper bowl rim. A pronounced interaction zone exists where the bowl vortex and the vortex above the step region contact one another. The relatively lean mixture located in this interaction zone forms with the fuel injected at the end of the main injection.

The last crank angle depicted in Figure 6, 30 CAD ATDC, occurs as the period of enhanced mixing controlled heat release with the stepped-lip bowl is nearing its end (see [4]). The prominent flow feature in the conventional bowl, the toroidal vortex, persists as the fuel-air mixture begins to exit the bowl. Mixture is also located in the outer portions of the squish region above the conventional bowl, but radial flow velocities in this region are low and do not act to displace the mixture in a substantial way. In the stepped-lip bowl, multiple recirculating structures remain intact. The upper, inner structure transports mixture from the squish region upward and inward, away from the step. The outer recirculation region has weakened, and mixture remains in the outermost portions of the squish region. A clear separation often remains between the mixture in the outer squish region and the mixture in the upper recirculation zone (fifth row, right column of Figure 6).

The spreading of mixture and turbulence near the cylinder head is analyzed by examination of simulation results in a horizontal (swirl-plane) cross-section located 1 mm below the cylinder head surface. In Figure 7, fuel-air equivalence ratio distributions are shown with a false color map and iso-contours of root-mean-square (RMS) velocity fluctuations (u') are used to indicate turbulence levels and locations. Black vectors indicate the direction, but not the magnitude, of the mean velocity field as it is projected onto the horizontal plane.

At a crank angle of 19.5 CAD ATDC (first row of Figure 7), the horizontal-plane mixture distributions are qualitatively similar: portions of each of the seven spray heads are visible for both the conventional and stepped-lip bowls. However, the velocity fields surrounding the spray heads above the stepped-lip bowl typically indicate a stronger divergent flow pattern than those above the conventional bowl. This is consistent with the above description that a portion of the spray heads penetrates outward through the squish region, and not upward toward the cylinder head. Turbulence levels in the spray heads are comparable for both piston geometries: the black iso-contour (corresponding to u' =3 m/s) envelops the spray heads, and higher turbulence levels are typically observed in the interior of the sprays.

The differences in horizontal-plane mixture and turbulence distributions above the two pistons become larger at 25 CAD ATDC (second row of Figure 7). The individual sprays have reached the outer portions of the bore, but remain as

FIGURE 7 Cross-sectional views of fuel-air equivalence ratio (color map), mean velocities (vectors) and RMS velocity fluctuations (black and grey iso-contours) in a plane located 1 mm below the cylinder head surface for the intermediate main injection timing. Port designations: Ex: exhaust; H: helical; T: tangential.

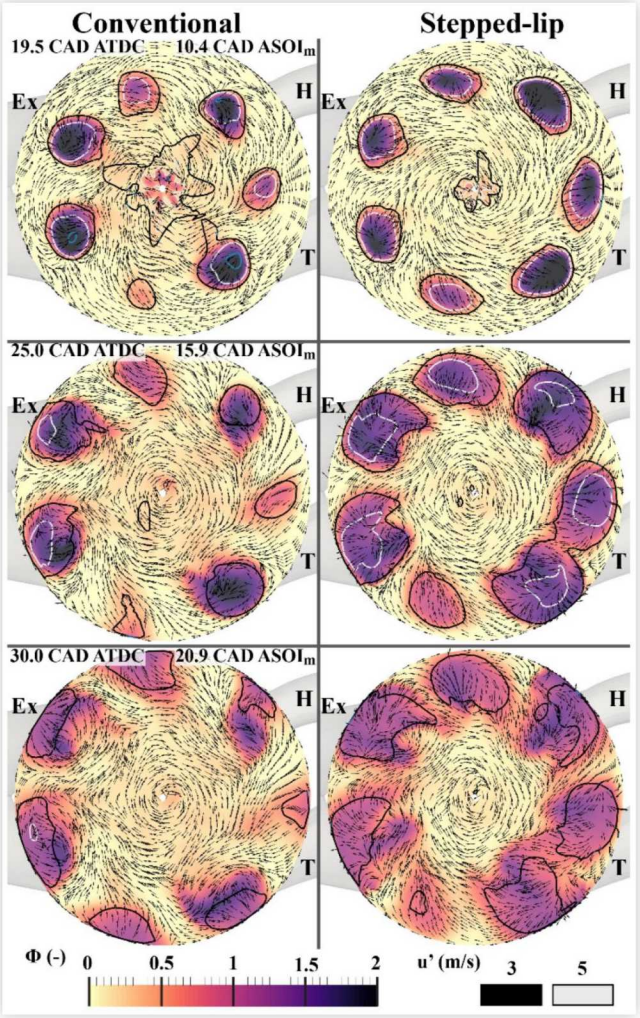

separate mixture clouds above the conventional bowl. Swirl has transported the mixture and has resulted in a limited amount of tangential spreading. With the stepped-lip bowl, the sprays have spread considerably. The formation of the two recirculation zones above the step and squish regions coincides with radial spreading of the mixture. Swirl further supports the tangential spreading, and the secondary sprays have begun to merge with one another. Turbulence levels have decreased more rapidly above the conventional bowl, as the grey iso-contours (corresponding to u' =5 m/s) have nearly disappeared. Above the stepped-lip piston, turbulence levels remain relatively high over a large portion of the spray heads: the grey iso-contours persist throughout most of the sprays. Additionally, u' iso-contours tend to follow the edges of the mixture clouds more closely above the stepped-lip piston. This co-location of steep fuel concentration gradients and elevated turbulence levels should foster turbulent fuel-air mixing and improve air utilization.

At 30 CAD ATDC, many of the secondary spray heads have merged with their neighbors above the stepped-lip bowl, and near-stoichiometric mixtures exist over a large portion of the squish region. The inward flow associated with the upper toroidal vortex continues to transport mixture toward the center of the combustion chamber. The degree of mixing above the conventional bowl is markedly less: the spray heads have still not merged with one another and very little inward transport has occurred because no organized flow structure has been formed to perform this work. Turbulence levels have continued to decrease in both cylinders, as the grey iso-contours have all but disappeared, but the highest turbulence regions are still distributed over a larger portion of the cutting plane above the stepped-lip bowl than for the conventional bowl.

The bowl geometries used in this study have a significant impact on efficiency and emissions for the intermediate injection timing, and simulation results reveal substantial differences in turbulent flow structure that result from spray-wall interactions. A summary of the pertinent features of the flows inside these two combustion chambers is given below, along with some additional insights from the literature.

With the conventional bowl, a nearly even splitting of fuel occurs at the bowl rim during the intermediate main injection: approximately half of the fuel is redirected downward into the bowl, and the remainder continues to propagate outward into the squish region. The redirection of fuel down into the bowl results in the formation of a large, long-lived toroidal vortex that is the dominant flow feature in this combustion system. The impingement process at the bowl rim imparts a small upward velocity to the portion of the sprays that initially penetrates into the squish region. However, the sustained delivery of outwardly directed momentum during the remainder of the main injection produces a primarily radial flow pattern in the squish region. Spreading of mixture and turbulence in the squish region is limited, and the spray heads are not observed to merge with one another.

The evolution of turbulent flow inside the stepped-lip combustion chamber is considerably more complex. The fuel sprays impinge directly on the stepped region, and most of the fuel remains above the spray axes. The small portion of the sprays that is redirected down into the bowl creates a toroidal vortex that is qualitatively similar to the one in the conventional bowl, but smaller. The larger portion of the sprays interacts with the conical surface of the step until it reaches the vertical surface of the upper bowl rim. The step and vertical surface impart a significant vertical component to the sprays as they separate from the bowl surface, penetrate as secondary sprays upward toward the cylinder head, and out into the squish region. The corner made by the step surface and the vertical upper rim may be similar to the "bump" used by Su et al. to create flow separation of a wall jet [29]. They demonstrate that the details of this geometric feature can have a dramatic impact on the behavior of the secondary jet [29, 30]. The secondary sprays travel upward and outward toward the cylinder head, and one hypothesis is that the interaction with the head is like that of a jet impinging on a wall. Impinging diesel sprays are reported to cause an increase in vapor and flame volume [31]. The secondary sprays above the step region appear to increase the volume of the sprays, as turbulence and mixture are spread both radially and tangentially along the head surface. Tangential spreading causes the sprays to merge with one another. As the sprays spread outward toward the cylinder wall, they are deflected downward. Similarly, the presence of the cylinder wall causes the flow to turn inward just above the top of the piston, and a recirculation flow pattern forms in the outermost portion of the squish region. Experimental evidence of this phenomenon has recently been produced, but the experimental results indicate that this flow structure forms earlier than what is predicted in this simulation [3]. The causes for this discrepancy are not well understood, but a likely factor is the lack of combustion-driven expansion in the simulation. In addition, a larger recirculation zone is formed above the bowl as momentum is directed inward by the interaction of the secondary sprays with the cylinder head. This flow structure is long-lived and energetic: it persists until after 40 CAD ATDC (not shown). The associated inward velocity is observed at many locations inboard of the region above the step (see Figure 7), and because it is observed in multiple vertical cutting planes (not shown), it is assumed to be a toroidal vortex. This vortex is responsible for transporting the mixture toward the centerline during the later stages of the cycle. It interacts with the toroidal vortex in the bowl, but the non-combusting simulations suggest that no significant fuel-air mixing takes place in the interface region. A combination of dual vortices has been previously reported in association with a stepped-lip combustion chamber [1, 32], and has been associated with enhanced heat release rates in the second half of combustion [11]. This explanation of the flow inside the stepped-lip combustion chamber is largely consistent with the description given by Iikubo et al. [33].

The Mechanism Responsible for the Formation of Recirculating Flow Structures above the Stepped-Lip Piston

The dual recirculating flow structures that form above the step and in the squish region are created because of interactions between the sprays and the combustion chamber surfaces, but it is unclear how the outward, downward momentum of the fuel injection is transformed to create recirculation in these regions above the piston. Most of the jet momentum is directed radially outward. Therefore, the simulation results are analyzed in the context of the Reynolds-averaged radial momentum equation, which is normalized by local velocity magnitude to facilitate comparison with cases for which spray velocities may be expected to differ.

$$\frac{1}{|\vec{u}|}\frac{\partial u_r}{\partial t} = \frac{\mu}{|\vec{u}|}\left(\frac{\partial}{\partial r}\left\{\frac{1}{r}\frac{\partial}{\partial r}\left(ru_r\right)\right\} + \frac{1}{r^2}\frac{\partial^2 u_r}{\partial \theta^2} + \frac{\partial^2 u_r}{\partial z^2} - \frac{2}{r^2}\frac{\partial u_\theta}{\partial \theta}\right)$$

$$+\frac{1}{\rho|\vec{u}|}\frac{\partial \tau_{ij}}{\partial r} + \frac{1}{|\vec{u}|}\frac{u_\theta^2}{r} + \frac{-1}{\rho|\vec{u}|}\frac{\partial p}{\partial r} + \left(-\frac{u_\theta}{r|\vec{u}|}\frac{\partial u_r}{\partial \theta} - \frac{u_r}{|\vec{u}|}\frac{\partial u_r}{\partial r} - \frac{u_z}{|\vec{u}|}\frac{\partial u_r}{\partial z}\right) \quad (2)$$

This form of the equation describes the normalized radial acceleration $\frac{1}{|\vec{u}|}\frac{\partial u_r}{\partial t}$ in a differential control volume as it depends on:

- Viscosity: $\frac{\mu}{|\vec{u}|}\left(\frac{\partial}{\partial r}\left\{\frac{1}{r}\frac{\partial}{\partial r}(ru_r)\right\}+\frac{1}{r^2}\frac{\partial^2 u_r}{\partial \theta^2}+\frac{\partial^2 u_r}{\partial z^2}-\frac{2}{r^2}\frac{\partial u_\theta}{\partial \theta}\right)$
- Turbulence: $\frac{1}{\rho|\vec{u}|}\frac{\partial \tau_{ij}}{\partial r}$
- Centrifugal force: $\frac{1}{|\vec{u}|}\frac{u_\theta^2}{r}$
- Radial pressure gradient: $\frac{-1}{\rho|\vec{u}|}\frac{\partial p}{\partial r}$
- Radial momentum convection: $-\frac{u_\theta}{r|\vec{u}|}\frac{\partial u_r}{\partial \theta}-\frac{u_r}{|\vec{u}|}\frac{\partial u_r}{\partial r}-\frac{u_z}{|\vec{u}|}\frac{\partial u_r}{\partial z}$

Because all the terms in Equation 2 have been normalized by the velocity magnitude, each term represents a normalized rate of radial acceleration. In this work, the rates are expressed in units of 1/CAD. The simulations are performed in cartesian coordinates, so many of the variables in Equation 2 are not available as direct outputs of the CFD simulation. Instead, the cylindrical terms are computed from available simulation output variables and their spatial derivatives. Each partial derivative is computed from simulation output variables; the necessary equations are derived in the Appendix. The terms of the normalized radial acceleration equation are evaluated in the computational domain and shown on a vertical cutting plane to establish the first order effects that drive the formation of each of the two recirculating flow structures above the stepped-lip piston. Results are shown for a single spray but represent the behavior of each spray in a general sense.

The velocity-normalized radial acceleration is shown in Figure 8 for four crank angles during and after the intermediate injection. The information depicted in these images represents the left-hand side of Equation 2. Red indicates regions of positive (outward) acceleration, whereas blue indicates regions with negative (inward) acceleration. The limits of the red and blue color scales are acceleration magnitudes of ±2/CAD, which correspond to a change in radial velocity equal to twice the local velocity magnitude within one crank angle degree. A black contour line is drawn to indicate the stoichiometric iso-contour and give a visual impression of the spray's location. The vertical cutting plane intersects one of the spray axes, and it is apparent that the radial acceleration behavior is heavily influenced by the spray's presence. In fact, the radial acceleration for the motored case (not shown) is insignificant compared to the injected cases. The crank angles depicted in the four images in Figure 8 represent several phases of the spray-wall interaction:

- 4.9 CAD $ASOI_{main}$: The spray penetrates outward and downward through the cylinder.
- 5.4 CAD $ASOI_{main}$: The spray begins to interact with the inner bowl rim.
- 7.9 CAD $ASOI_{main}$: Shortly before the end of the main injection, the secondary spray is separating from the piston surface.

FIGURE 8 Vertical-plane view of velocity-normalized radial-acceleration distributions on the spray axis for three crank angles for the intermediate injection timing. Red regions indicate positive (outward) acceleration, whereas blue regions indicate negative (inward) acceleration. The stoichiometric iso-contour is shown with a black line. These images represent the left-hand side of Equation 2.

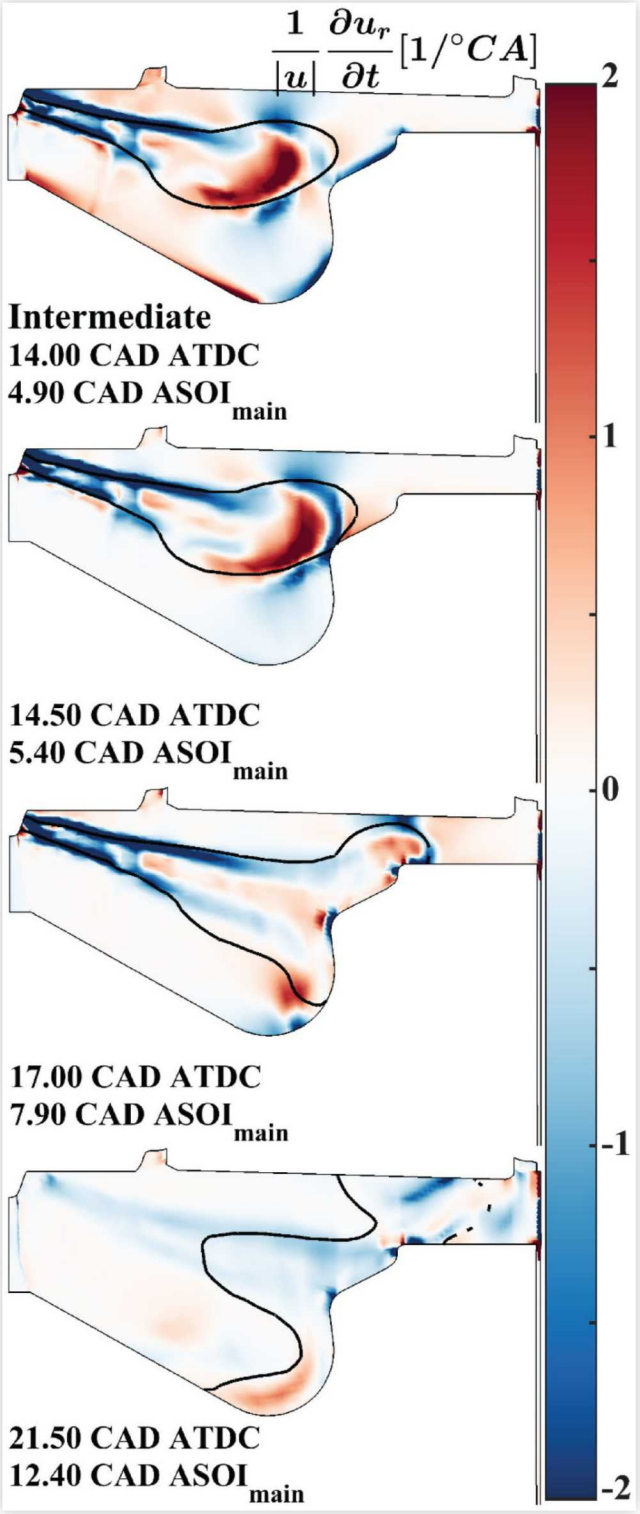

- 12.4 CAD $ASOI_{main}$: After the end of the main injection, radial acceleration magnitudes are decreasing and recirculating flow patterns are beginning to become evident.

The top image in Figure 8 indicates strong radial deceleration in the upstream portion of the spray, seen as dark blue bands oriented parallel to the edges of the spray. This is consistent with low-momentum air being entrained into the high-velocity fuel jet, thereby decreasing the spray's velocity. A prominent region of positive (outward) radial acceleration is observed in the head of the spray. Two small regions of negative radial acceleration are observed above and below the spray head, and a third small region of negative radial deceleration is beginning to form near the tip of the spray. The faint red region above the inner bowl rim indicates outward acceleration in front of the spray. The dark blue regions along the step and near the bottom of the bowl are very short-lived; they are believed to be an artifact of changes to the moving mesh and can likely be ignored.

The second image in Figure 8 shows the radial acceleration 0.5 CAD after the top image. The spray penetration has continued, and the spray is beginning to interact with the wall. Much of the spray structure remains intact, but the regions of negative acceleration above and below the spray have merged with the one in front of it. The negative radial acceleration near the lower bowl rim increases significantly in a very short time as the spray begins to impinge on the bowl wall. The faint red region in front of the spray and above the step has increased in size and intensity; the outward acceleration in this region is increasing as the spray begins to split.

As depicted in Figure 6, the secondary spray travels along the step surface until it is deflected upward by the outer bowl rim, at which point it penetrates upward and outward away from the piston surface. The radial acceleration associated with this phase of the spray-wall interaction is depicted in the third image in Figure 8. Above the outer bowl rim, the outward acceleration of the secondary spray is visible as a red region near the leading edge of the secondary spray. The regions of negative radial acceleration continue to move with the periphery of the spray head, and the negative acceleration region near the cylinder head is similar in size to the positive region below it. The fluid in front of the spray begins to exhibit positive radial acceleration as the secondary spray first penetrates the squish region.

The secondary spray continues to penetrate upward and outward into the squish region after the end of injection, but the outward acceleration associated with this penetration decreases (see bottom image of Figure 8). Negative acceleration persists near the cylinder head, and the spray - as indicated by the black stoichiometric iso-contour - has spread inward along the cylinder head. A negative acceleration region has formed in the outer portion of the squish region below the secondary spray. This is consistent with the formation of the outer recirculation zone as the secondary spray changes direction downward along the cylinder and inward above the piston surface, as shown in Figure 6.

The images in Figure 8 represent the left-hand side of Equation 2; the terms on the right-hand side must account for the observed radial acceleration behavior. The right-hand-side terms are shown in the order they appear in Equation 2 in Figure 9 and Figure 10. The contributions to radial acceleration due to viscosity, turbulence, and the radial pressure gradient are depicted in Figure 9 at 7.9 CAD $ASOI_{main}$. Note that the color scaling is identical to what is shown in Figure 8.

FIGURE 9 Vertical-plane view of contributions to radial acceleration due to viscous forces (top), turbulence (second), centrifugal force (third) and pressure gradients (bottom) on the spray axis shortly before the end of the intermediate injection. The color scale and stoichiometric iso-contours are the same as in Figure 8. Adverse radial pressure gradients are indicated in the bottom image as blue regions. These images, along with the ones shown in Figure 10, represent the right-hand side of Equation 2.

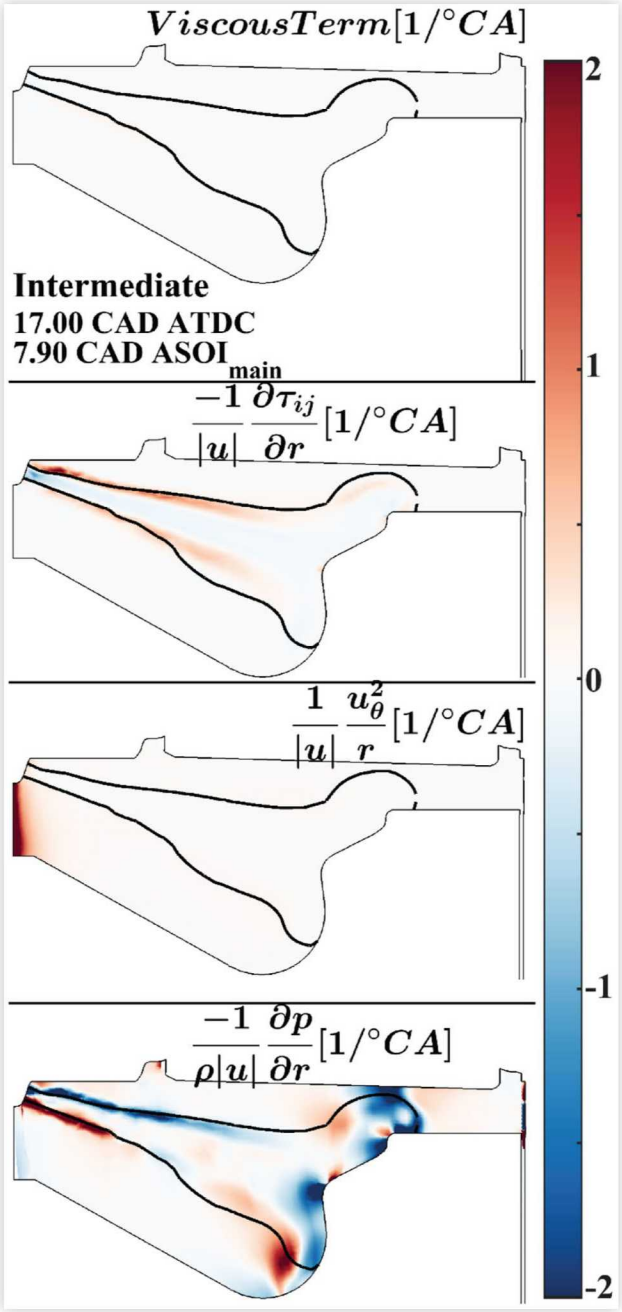

FIGURE 10 Vertical-plane view of contributions to radial acceleration due to azimuthal convection (top), radial convection (middle), and vertical convection (bottom) on the spray axis shortly before the end of the intermediate main injection. A small illustration shows the pertinent surfaces of a differential control volume for each convective term. These images represent terms on the right-hand side of Equation 2.

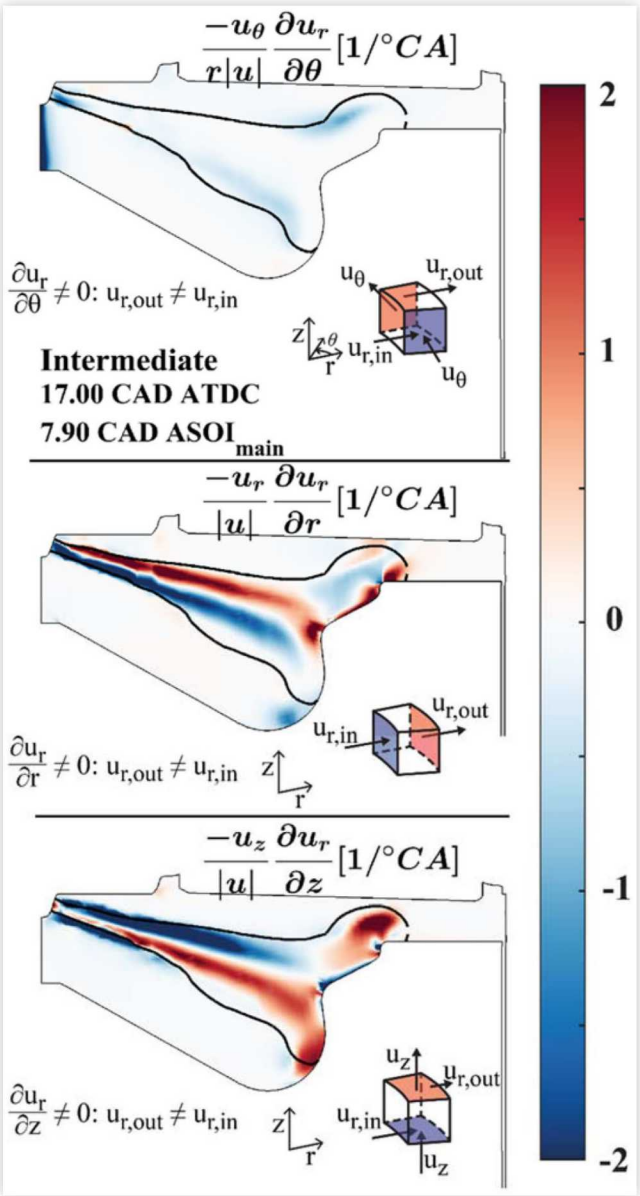

The top image demonstrates that viscous forces are insignificant; the assumption of inviscid flow is highly unlikely to impact the prediction of the recirculation zones. The effects of turbulent forces (the second image in Figure 9) are primarily visible as faint bands of positive acceleration along the periphery of the spray, particularly in the upstream regions. While these forces may potentially affect the shape of the upstream portion of the spray, they do not significantly impact the behavior shown in Figure 8. Centrifugal force impacts radial acceleration only near the center of the chamber, as seen in the third image in Figure 9. This acceleration is attributed to swirl asymmetry, but does not impact the evolution of flow above the step and in the squish region.

The contribution of the radial pressure gradient, shown at the bottom of Figure 9, is significant throughout the spray, but particularly in the region of interest above the step and in the squish region. The blue regions represent areas in which adverse pressure gradients act to accelerate the flow inward. Indeed, the region above the outer rim of the piston is dominated by these adverse pressure gradients; this will be discussed in more detail later.

The remaining three terms on the right-hand side of Equation 2 describe the effect of radial-momentum convection on radial acceleration, and are depicted in Figure 10 at 7.9 CAD $ASOI_{main}$.

The top image of Figure 10 depicts the contribution of azimuthal convection. It has a noticeable deceleration effect just inside the periphery of the spray, but it is insignificant in the squish region. It is not responsible for the behavior described in Figure 8. The second convective term (the middle image in Figure 10) describes the transport of radial momentum in the radial direction; it is present throughout the spray. However, it counteracts the behavior shown in Figure 8 for the outward radial acceleration of the spray into the squish region and inward acceleration along the cylinder head. This means that radial convection of radial momentum acts to hinder the formation of the recirculating flow structures shown in Figure 6, but it is not a strong enough effect to prevent their formation for the intermediate injection timing. The final term on the right-hand side of Equation 2 is the vertical convective term; it is shown at the bottom of Figure 10. Inspection of Figure 9 and Figure 10 reveals that the vertical convection of radial momentum is the only term responsible for the outward acceleration of the secondary spray into the squish region shown in Figure 8. The interpretation of this vertical convection term is as follows: the step acts to impart an upward velocity on the outwardly penetrating spray, and the radial velocity decreases away from the center of the spray. As a result, the fluid in the entrance of the squish region accelerates outward as the vertical component of the flow introduces fluid with an increasingly large radial velocity into the control volume.

The radial acceleration behavior observed above the step and in the squish region is dominated by two factors: vertical convection of radial momentum, and adverse radial pressure gradients. Figure 11 shows velocity vectors overlaid on the vertical convection term to demonstrate that this term creates outward acceleration in the squish region that is responsible for the formation of the outer recirculation zone. The radial pressure gradient is responsible for inward acceleration along the cylinder head and in the outer, lower portion of the squish region. Figure 12 depicts how adverse pressure gradients act to slow the secondary spray as it penetrates out into the squish region, but the pressure gradient is insufficient to stop the spray's progress. However, the vertical convection of outward radial momentum is diminished near the cylinder head, and the inward forces associated with the adverse pressure gradient prevail. The flow near the cylinder head is driven inward by the adverse radial pressure gradient.

To better illustrate the cause of the adverse radial pressure gradients responsible for the inward flow along the cylinder

FIGURE 11 Vertical-plane view of the contribution to radial acceleration due to vertical convection of radial momentum on the spray axis for three crank angles during and after the intermediate main injection. Velocity vectors are projected onto the vertical plane; velocity magnitudes less than 10 m/s are not shown. Vertical convection of radial momentum drives the secondary spray's upward and outward acceleration into the squish region.

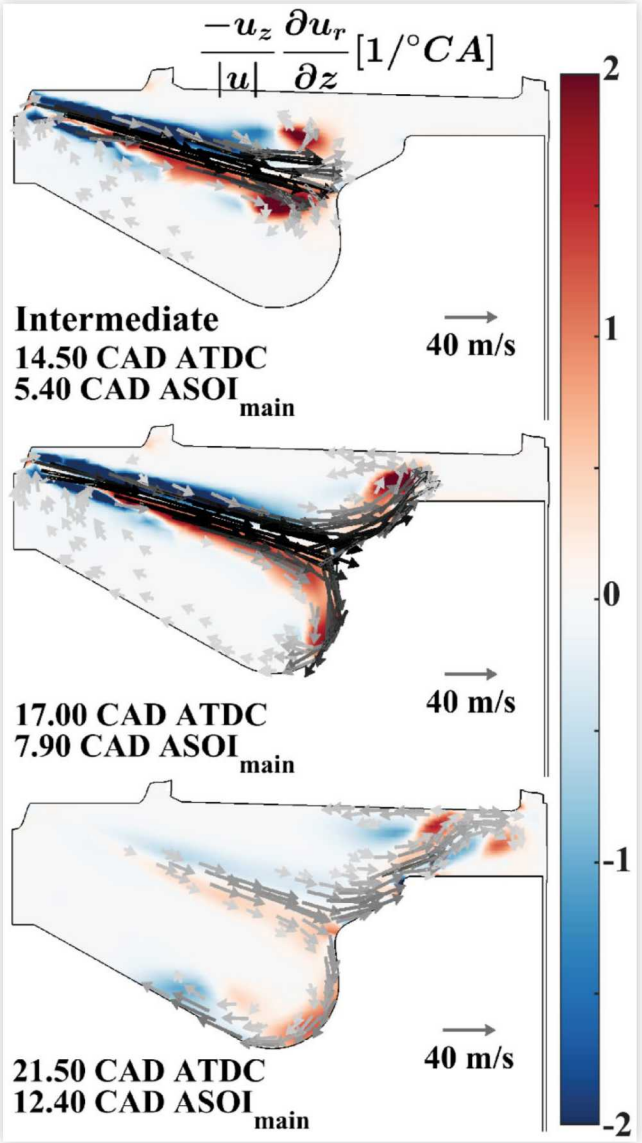

FIGURE 12 Vertical-plane view of the contribution to radial acceleration due to the radial pressure gradient on the spray axis for three crank angles during and after the intermediate main injection. Velocity vectors are projected onto the vertical plane; velocity magnitudes less than 10 m/s are not shown. Adverse radial pressure gradients (blue regions) are responsible for the inward acceleration of flow near the cylinder head and in the outer portion of the squish region.

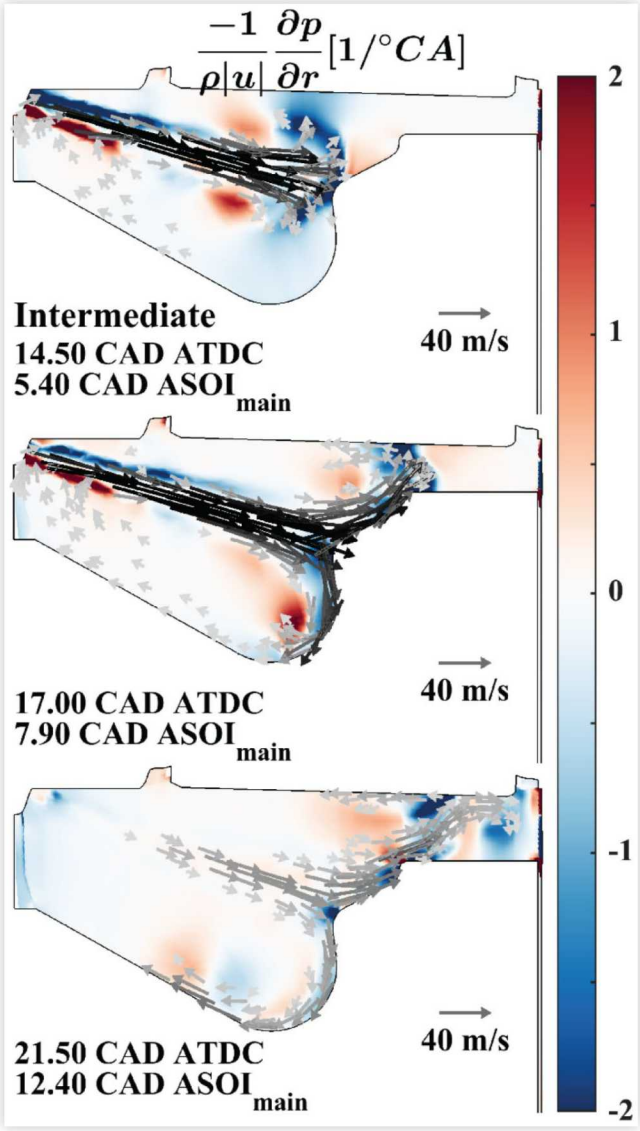

head, the relative pressure is computed as the difference between the local pressure and the volume-weighted average cylinder pressure, p_{cyl}. The relative pressure is shown in Figure 13 for a horizontal (swirl) plane located 2 mm beneath the cylinder head. Iso-contours for fuel-air equivalence ratios of 1.0 and 0.5 are shown in black and grey, respectively. Adverse radial pressure gradients appear as transitions from dark blue to white and from white to dark red as radius increases.

An analysis of Equation 2 for motored operation with a swirl ratio of 2.2 suggests that the pressure differential resulting from centrifugal force is on the order of 20 Pa: swirl does not have a measurable impact on the relative pressure distributions shown in Figure 13. Rather, the increase in pressure observed in the squish region is caused by the fuel injection. Low pressures in the center of the chamber are likely associated with entrainment flow, but the regions of highest relative pressure are in front of the sprays as they penetrate outward into the cylinder and upward and outward as they interact with the step (seen in the top image of Figure 13). The penetrating sprays displace these high-pressure zones into the squish region, where they stagnate at the cylinder liner. These pressure differences are strongest near the end of the injection (see middle of Figure 13), but dissipate relatively quickly after the injection ends (see bottom of Figure 13).

FIGURE 13 Swirl-plane relative pressure distributions for a plane located 2 mm below the cylinder head for three crank angles during and after the intermediate main injection. Iso-contours are shown for equivalence ratios of 1.0 (black) and 0.5 (grey). Adverse pressure gradients above the step are caused by the combination of decreased pressures within the sprays and the increased pressure in front of each spray.

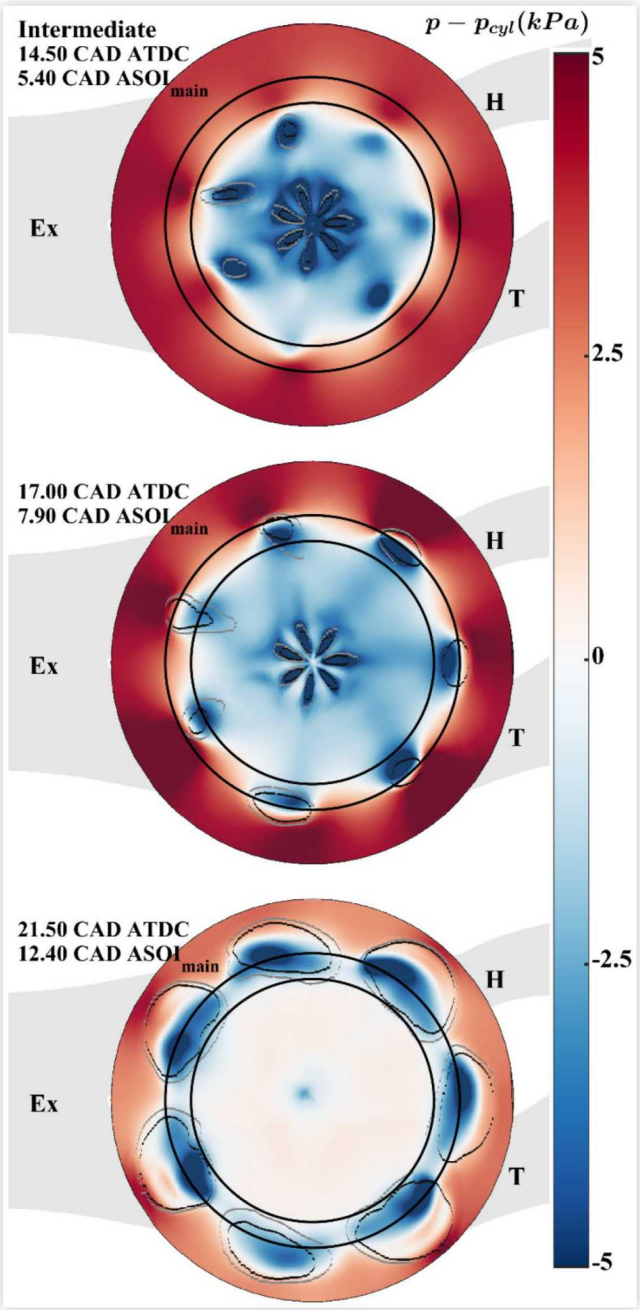

The physics responsible for the formation of each of the two recirculation zones above the stepped-lip piston are distinct. The outer recirculation zone forms in the squish region as secondary spray momentum is redirected upward and the fluid in the squish region is accelerated outward. As the secondary spray approaches the liner, adverse pressure gradients act to turn it downward and inward, and the recirculation flow pattern is established. The recirculation zone that forms nearer the center of the chamber is created by adverse pressure gradients near the cylinder head. These pressure gradients result from the outward penetration of the secondary sprays and the regions of increased pressure that form in front of them. The high pressure regions are transported into the squish region, where they stagnate on the cylinder wall. The forces associated with the adverse pressure gradient prevail near the cylinder head, so the flow nearest the cylinder head is driven inward. Continuity dictates that this flow will eventually be forced downward as it approaches the center of the combustion chamber, and the remaining outward flow in what remains of the original spray helps to establish this recirculation zone late in the cycle.

Injection Timing Effects

The mechanisms by which beneficial recirculating flow structures form above the stepped-lip piston have been established for the intermediate injection timing. The efficiency and emissions benefits associated with these flow structures are diminished for the near-TDC main injection timing (see Figure 1). Indeed, the simulation results shown in Figure 14 indicate that for the near-TDC injection timing, energetic, long-lived recirculation zones are not observed above the step or in the squish region. Recent experimental results provide supporting evidence that for the near-TDC injection timing, the recirculation pattern in the squish region is weaker and shorter-lived than for the intermediate injection timing [3]. The flow topology in the stepped-lip bowl has changed significantly from what is predicted for the intermediate main injection timing (Figure 6); the bowl vortex appears to be the only recirculating flow structure. In contrast, the flow in the conventional, re-entrant piston bowl is affected by injection timing to a much smaller extent: the flow topology continues to be dominated by the bowl vortex described above. This result supports the hypothesis that the efficiency and emissions advantages of the stepped-lip piston over the conventional re-entrant piston are associated with the intensity and longevity of these recirculating flow structures. Their formation is sensitive to injection timing.

Changing injection timing affects spray dynamics and spray-wall interactions in several ways. Downward piston motion during the expansion stroke acts to decrease bulk gas density. Decreased ambient density alters the exchange of momentum between the jet and the bulk gas, and decreases the amount of air entrainment, thus reducing the spray velocity to a lesser extent. Additionally, the change in piston position with changing injection timing means that the spray targeting changes. These effects and their impact on the formation of the recirculation zones above the stepped-lip piston are described below.

Bulk Gas Density and Spray Velocity The effects of ambient density on spray penetration are well established in the literature [34]. The spray spreading angle model used in this study, which dictates near-field air entrainment into the sprays, dynamically varies the spreading angle as ambient density changes (see [17] for details). In the absence of fuel

FIGURE 14 Vertical cross sectional view of fuel-air equivalence ratio and velocity fields projected onto the cutting plane at the spray axis for the near-TDC injection timing. The crank angles relative to the start of main injection for each row are comparable to those shown in Figure 6. All images have been compressed horizontally to fit in the column. Yellow arrows have been added to indicate trends in spray propagation.

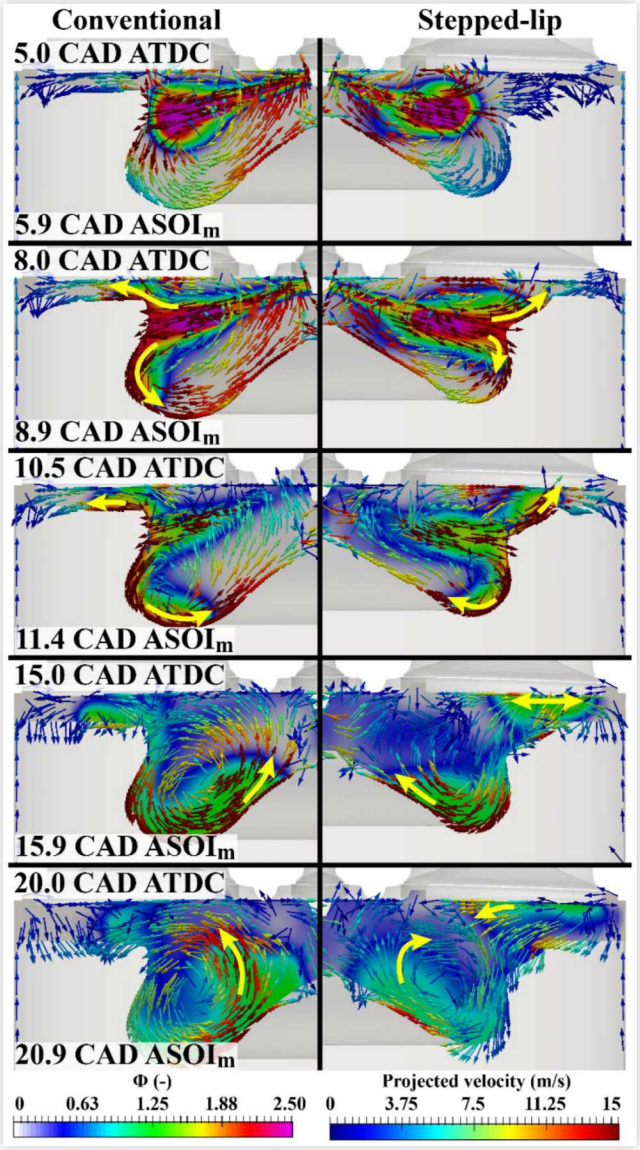

injection, the bulk gas density decreases from approximately 20.5 kg/m^3 at 5 CAD ATDC (during the near-TDC main injection) to 16.1 kg/m^3 at 15 CAD ATDC (during the intermediate main injection). This corresponds to a modeled change in spreading angle from approximately 15° to approximately 13° from the near-TDC to the intermediate injection timings. The spray modeling approach implicitly considers the momentum exchange between the sprays and the ambient gas [17]. The increase in gas density when changing from the intermediate to the near-TDC injection timing is expected to result in increased air entrainment into the sprays, and decreased spray penetration velocities into the cylinder.

FIGURE 15 Velocity magnitudes for the near-TDC (top) and intermediate (bottom) main injection timings. The images are both shown at 7.4 CAD ASOI$_{main}$ for a vertical plane containing the spray axis. The stoichiometric iso-contours are shown with black lines. Note the differences in velocity distribution relative to the extent of the fuel vapor.

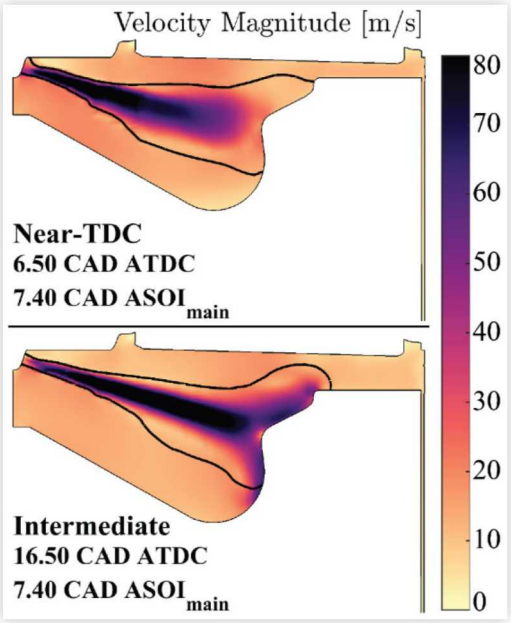

Figure 15 shows velocity magnitude distributions 7.4 CAD ASOI$_{main}$ for each injection timing. The results confirm that simulated spray penetration is faster for the intermediate injection timing: the high-velocity core of the spray has penetrated much farther for the intermediate injection timing. Note, however, that the stoichiometric iso-contour precedes the near-TDC spray by a greater extent than for the intermediate injection timing. The fuel spray is narrower and more compactly distributed for the intermediate injection timing; this prediction is consistent with lower air entrainment rates and decreased momentum exchange with the ambient gas.

Spray Targeting, Fuel Splitting, and Momentum Distribution Another important effect of changing injection timing is altered spray targeting throughout the injection event. Spray targeting is depicted in Figure 16 for the near-TDC and intermediate injection timings. Piston positions are shown at three times in each case: at the start of the main injection, at the approximate start of fuel vapor impingement on the bowl rim (as observed in the CFD results), and at the end of the main injection. The piston moves downward by approximately 2.7 mm during the intermediate main injection. The spray axis intersects the lower portion of the conical step surface for much of the injection event. On the contrary, the piston position changes by less than 0.8 mm throughout the near-TDC main injection event, so the spray targeting is nearly static. The spray axis intersects the lower portion of the bowl, several mm below the inner bowl rim.

While Figure 16 describes theoretical spray targeting scenarios, several factors will influence the actual penetration

FIGURE 16 Spray targeting diagrams for the near-TDC and intermediate injection timings. Three instants in time are shown at each injection timing: the start of the main injection (SOI_{main}); the approximate time of spray impingement on the bowl surface, and the end of the main injection (EOI_{main}).

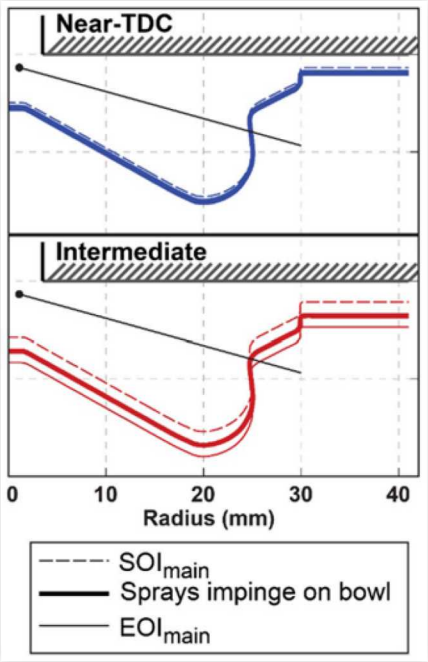

FIGURE 17 Portion of total in-cylinder fuel located above the spray axes as a function of crank angle for the stepped-lip piston at the near-TDC (blue open circles) and intermediate (red filled circles) main injection timings. A value of 0.5 represents even splitting above and below the spray axes.

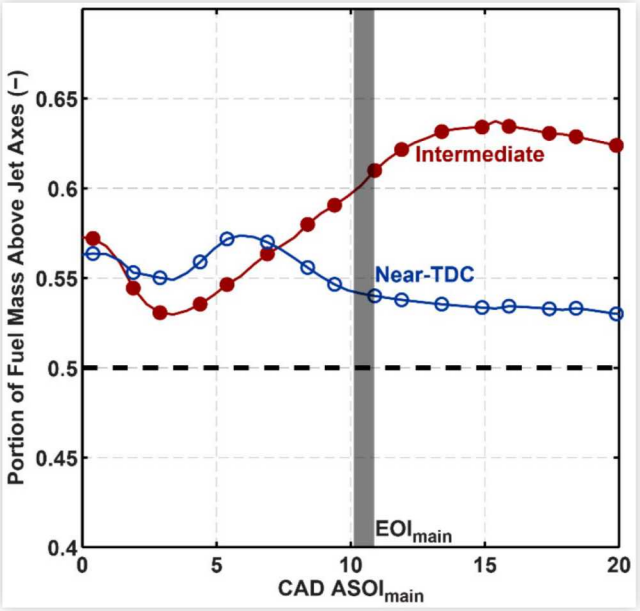

angle of the sprays. The proximity of the sprays to the fire deck leads to upward deflection of the sprays due to the Coandă effect [35]. Furthermore, squish and reverse squish flows, their interactions with swirling flows, and the resulting toroidal vortex structure can also influence spray propagation. Finally, the asymmetrical flow topology that exists near TDC (measured experimentally and predicted by simulations [26, 36]) may deflect each spray to a different degree.

Because the piston remains near its highest position for the duration of the near-TDC main injection (Figure 16), a nearly constant fuel splitting ratio may be expected to occur as the fuel sprays interact with the slowly moving piston. The fuel splitting behavior for both the near-TDC and intermediate main injections is depicted in Figure 17. Indeed, the proportion of fuel above the spray axes remains near 55% for the near-TDC injection timing; it gradually decreases after the end of the main injection. Fuel is more effectively transported to the upper portion of the combustion chamber during and after the intermediate main injection.

The combined effects of changing bulk gas density and fuel spray splitting on the secondary spray momentum are assessed through analysis of the CFD results. To this end, a planar control surface is defined at the top surface of the piston; the associated non-inertial reference frame moves with the piston. The cell-centered, three-dimensional density and velocity fields are mapped onto this surface. For each time for which simulation results have been exported, three-dimensional density and velocity fields are computed on the control surface. This control surface is represented by the faces in a triangulation whose set of nodes is made by the intersection of the computational cell edges (depicted in Figure 2) and the horizontal control surface [37]. Momentum flux $\dot{\varphi}_z$ is computed through each face at each time step as follows:

$$\dot{\varphi}_z = \rho w \left(\vec{u} - \vec{v}_p \right) \cdot \hat{n} \tag{3}$$

ρ is the density
$\vec{u}$ is the gas velocity
$\vec{v}_p$ is the piston velocity
$\hat{n}$ is the control surface unit normal, a vertical unit vector
w is the vertical velocity component within a triangulated cell

The summation of the momentum fluxes over all the face areas yields the vertical momentum flow rate $\dot{p}_z$:

$$\dot{p}_z = \sum_{CS} \dot{\varphi}_z \, A_f \tag{4}$$

The vertical momentum flux distributions are shown in Figure 18 for both piston geometries at approximately 8.9 CAD $ASOI_{main}$. Note that the vertical momentum flux through this surface is always positive: a downward flux of negative momentum has the same effect as an upward flux of positive momentum. The momentum flux "background" associated with squish and reverse squish flows is negligible compared to the momentum flux in the fuel jets. Momentum flux in the center of the chamber is primarily associated with the downward propagation of the sprays; the entrainment flow does not contribute significantly to vertical momentum flux. The momentum flux associated with the secondary sprays flowing up out of the bowl is visible at the outer bowl rim. For the intermediate injection timing, these regions of high momentum flux are confined to thin annular segments,

FIGURE 18 Momentum flux through the horizontal control surface for both the near-TDC injection timing (left) and intermediate injection timing (right). Both images show the momentum flux approximately 8.9 CAD after the start of the main injection.

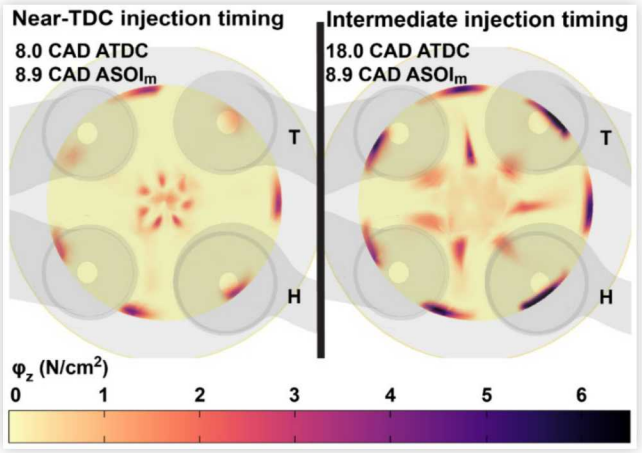

whereas the regions of highest momentum flux are smaller and distributed over a larger radial extent for the near-TDC injection timing. For any given spray, the peak upward momentum flux near the step is considerably higher for the intermediate injection timing.

The total vertical momentum flow is expressed as a dimensionless quantity that is normalized by the momentum delivered by the largest source of momentum: the main injection. For this, the average momentum flow-rate is computed at the injector nozzle exit:

$$\bar{p}_{inj} = \frac{\int_{t_{SOIm}}^{t_{EOIm}} \dot{m}_{inj} v_{inj} dt}{t_{EOIm} - t_{SOIm}} \tag{5}$$

$\dot{m}_{inj}$ is the rate of injection (as shown in Figure 3)
v_{inj} is the injection velocity, computed as:

$$v_{inj} = \frac{\dot{m}_{inj}}{C_d \rho_f A_{nozzle}} \tag{6}$$

C_d is the nozzle discharge coefficient, assumed to be 0.8
ρ_f is the density of the liquid fuel, taken to be 780 kg/m^3.
A_{nozzle} is the combined cross sectional area of all seven nozzle holes

The dimensionless vertical momentum flow rate through the control surface is defined as:

$$p_z^* = \frac{\dot{p}_z}{\bar{p}_{inj}} \tag{7}$$

Figure 19 shows p_z^* for both injection timings and associated with both downward and upward flow through the control surface. As seen in Figure 6 and Figure 14, the sprays begin to interact with the stepped-lip bowl between approximately 6 and 9 CAD after the start of the main injection. Before this point, the flow rate of momentum associated with the upward mass flow increases relatively slowly, albeit faster for the intermediate injection timing. This is attributed to

FIGURE 19 Dimensionless vertical momentum flow rate through the horizontal control surface (shown at top right) vs. CAD after SOI_{main}. Filled symbols correspond to upward mass flow and open symbols represent downward (negative) mass flow.

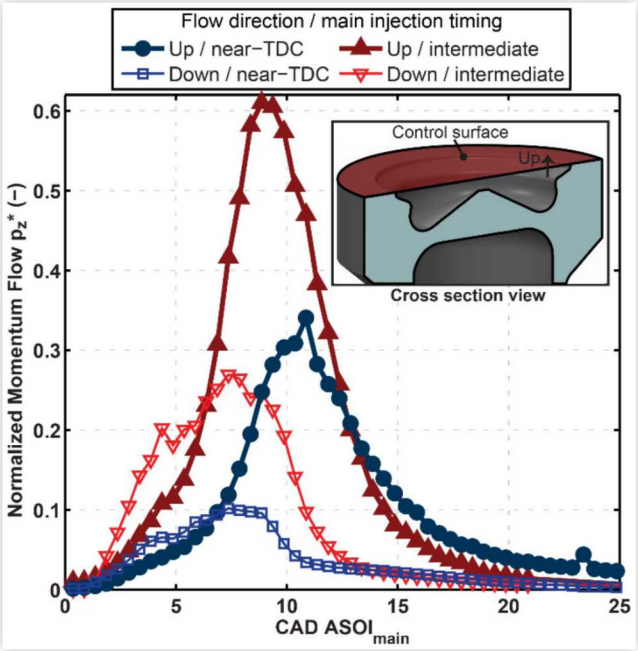

entrainment flow in the center of the cylinder and around the periphery of the sprays, and possibly to differences in the locations of the control surface relative to the fuel injector. The interaction with the step results in a significant increase in upward momentum flow through the control surface. For the intermediate injection timing, the peak upward momentum flow rate is more than 60% of the average momentum flow-rate provided by the fuel injection. The peak value is reached 2 CAD earlier, and is 80% higher than for the near-TDC injection timing. The reason for the earlier phasing of the momentum flow peak for the intermediate injection timing is not known, but it is consistent with faster spray penetration due to lower bulk gas densities at later crank angles.

Impact on Spray Structure and the Evolution of Radial Acceleration At the intermediate main injection timing, velocities within the sprays are higher and the delivery of momentum to the squish region is significantly advanced relative to the start of the main injection, when compared with the near-TDC main injection timing. The secondary sprays separate from the piston bowl later relative to the start of the near-TDC main injection, but it is unknown if the mechanisms that create recirculating flow structures for the intermediate injection timing are changed for the near-TDC injection timing. The radial acceleration distribution for the near-TDC injection timing is shown in Figure 20 for a vertical cutting plane at three crank angles during and after the main injection. The crank angles were chosen to facilitate comparison with the evolution of radial acceleration for the intermediate injection timing (Figure 8).

FIGURE 20 Vertical-plane view of velocity-normalized radial-acceleration distributions on the spray axis for three crank angles for the near-TDC injection timing. Red regions indicate positive (outward) acceleration, whereas blue regions indicate negative (inward) acceleration. The stoichiometric iso-contour is shown with a black line. Note the similarities in spray structure to the intermediate injection timing case (Figure 8).

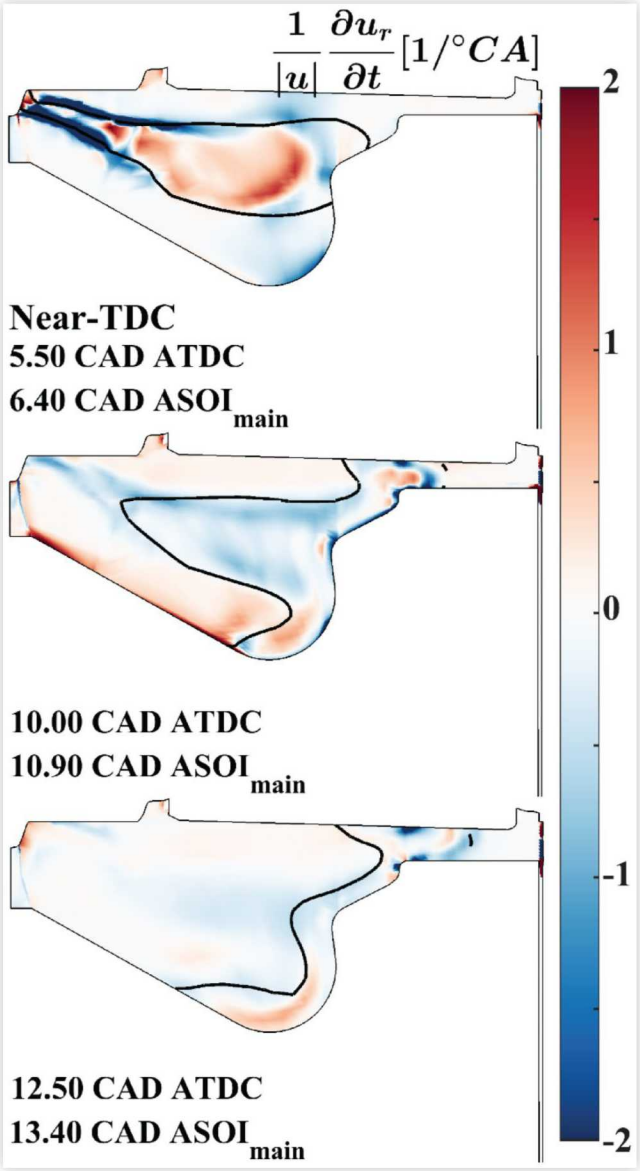

The mechanism by which the secondary spray accelerates out into the squish region appears to be qualitatively unaffected by the injection timing, as the radial acceleration distributions depicted in Figure 20 share many features with the intermediate injection timing (Figure 8). A region of outward acceleration is observed between the top piston surface and the cylinder head (middle image of Figure 20). Negative acceleration regions are observed near the cylinder head and just above the piston surface. The secondary spray penetrates upward and inward through the squish region (bottom image of Figure 20). However, since the spray velocities are significantly lower for the near-TDC injection timing, much of the development of the secondary spray takes place after the main injection has ended. Unlike for the intermediate injection timing, a continued supply of momentum from the injection is not available to drive the flow evolution above the step and in the squish regions. For these reasons, the secondary spray is considerably less energetic for the near-TDC injection timing than for the intermediate injection timing.

General Discussion

The fundamental mechanisms that create beneficial recirculating flow structures above the stepped-lip piston do not appear to change between the intermediate and main injection timings. Instead, the spray velocity and the distribution of momentum within the sprays is altered by the change in ambient density as injection timing is varied. For the intermediate injection timing, the spray quickly interacts with the step and the secondary spray separates from the outer bowl rim before the end of the main injection. For the near-TDC injection timing, the slower secondary spray separates from the piston later relative to the start of injection. This implies that while the fundamental mechanism that forms recirculation zones above the stepped-lip bowl may exist for a range of injection timings, secondary spray velocities and the phasing at which the mechanism is activated relative to the start of injection determine its efficacy at creating long-lived, energetic vortices. For the near-TDC injection timing, spray velocities may be too low, and the secondary spray separation may occur too late to have a beneficial effect on turbulent mixing, efficiency, and air utilization. The data shown in Figure 1 are consistent with this hypothesis, but further study will be necessary to confirm this.

While much has been learned about the ways in which stepped-lip pistons can enhance mixing, the impacts of several combustion system design/calibration parameters are still not well understood. The results of this work suggest that the optimization of a stepped-lip combustion system requires consideration of the shape and velocity of the sprays as they interact with the piston geometry. Future simulations will include variations in intake pressure and therefore in ambient density at the time of injection, to isolate ambient density / spray velocity effects from spray targeting effects. This will provide deeper understanding of spray targeting's effect on the redirection of spray momentum. The relative importance of swirl in this combustion system is not well documented. While centrifugal forces do not appear to play a role in the formation of vertical-plane rotational structures above the stepped-lip piston (see Figure 9), the stepped-lip piston retains a re-entrant bowl feature that likely depends on swirl for late-cycle turbulence generation [7]. Furthermore, sensitivities of combustion system behavior to details of the stepped-lip bowl profile or spray targeting parameters such as injector opening angle are not well characterized. This study has been performed for a single engine speed and load, and under non-combusting conditions. The effects of injection duration and combustion-driven expansion will therefore also be the focus of future studies. This work establishes a fundamental, scientifically based framework within which such variations can be analyzed.

Summary/Conclusions

Stepped-lip diesel piston bowls are often credited with efficiency and emissions advantages over conventional, re-entrant piston bowls, but recent experimental results indicate that these benefits depend on main injection timing. In this study, CFD simulations are performed to provide insight into differences in turbulent flow structure for a conventional, re-entrant piston bowl and a stepped-lip piston bowl in a small-bore diesel engine at two injection timings. Analysis of the CFD results provides a new understanding of the mechanisms by which beneficial recirculation zones form above the stepped-lip piston and the impact of injection timing on turbulent flow evolution. The findings and conclusions of this study are as follows:

- The appearance of two energetic, long-lived recirculation zones above the piston for the intermediate main injection timing coincides with experiments showing reduced soot emissions and faster mixing-controlled heat-release rates compared to operation with the conventional bowl. These recirculation zones are predicted to be weaker and short-lived with the stepped-lip piston for the near-TDC main injection timing, where experimental data show diminished advantages with the stepped-lip bowl.
- The interaction of the fuel sprays with the stepped-lip piston results in division of the fuel into the bowl and into the upper portion of the chamber. The conical step surface imparts a significant upward velocity to the secondary spray that penetrates along the step surface and separates from the piston at the outer bowl rim.
- Two factors drive radial acceleration of the secondary spray above the stepped-lip piston and result in the formation of recirculating flow structures. Vertical convection of the secondary sprays' radial momentum drives the formation of the recirculation zone in the squish region. Adverse radial pressure gradients form in front of the penetrating sprays and drive the uppermost portion of the secondary spray inward along the cylinder head surface, supporting the formation of the inner, upper recirculation zone.
- Vertical convection of radial momentum and adverse radial pressure gradients do exist for the near-TDC main injection timing, but they do not result in the formation of vertical plane vortices. The primary effect of changing injection timing appears to be to change ambient density and thereby the rate at which air is entrained into the sprays. This alters the velocity and momentum of the sprays, and changes the time relative to the start of injection at which the sprays interact with the piston bowl. This may be a contributing factor to the absence of these beneficial flow structures at the near-TDC injection timing.
- Advancing the injection timing results in slower sprays that interact with the step later and with less energy. It is believed that the secondary sprays are therefore unable to form energetic recirculating flow structures in time to result in efficiency and emissions advantages over the conventional, re-entrant piston at the near-TDC injection timing.

References

1. Crosse, J., "Going Clean-Off Highway," *Ricardo Quarterly Review* Q2, 2010.
2. Styron, J., Baldwin, B., Fulton, B., Ives, D. et al., "Ford 2011 6.7L Power Stroke® Diesel Engine Combustion System Development," SAE Technical Paper 2011-01-0415, 2011, doi:10.4271/2011-01-0415.
3. Zha, K., Busch, S., Warey, A., Peterson, R.C. et al., "A Study of Piston Geometry Effects on Late-Stage Combustion in a Light-Duty Optical Diesel Engine Using Combustion Image Velocimetry," SAE Technical Paper 2018-01-0230, 2018, doi:10.4271/2018-01-0230.
4. Busch, S., Zha, K., Perini, F., Reitz, R. et al., "Experimental and Numerical Studies of Bowl Geometry Impacts on Thermal Efficiency in a Light-Duty Diesel Engine," SAE Technical Paper 2018-01-0228, 2018.
5. Arcoumanis, C., Bicen, A.F., and Whitelaw, J.H., "Squish and Swirl-Squish Interaction in Motored Model Engines," *Journal of Fluids Engineering* 105(1):105-112, 1983, doi:10.1115/1.3240925.
6. Miles, P.C., RempelEwert, B.H., and Reitz, R.D., "Squish-Swirl and Injection-Swirl Interaction in Direct-Injection Diesel Engines," presented at *the ICE2003 6th International Conference on Engines for Automobiles*, Capri, Italy, 9/14/2003-9/19/2003.
7. Miles, P.C., Megerle, M., Hammer, J., Nagel, Z. et al., "Late-Cycle Turbulence Generation in Swirl-Supported, Direct-Injection Diesel Engines," SAE Technical Paper 2002-01-0891, 2002, doi:10.4271/2002-01-0891.
8. Miles, P.C., Turbulent Flow Structure in Direct-Injection, Swirl-Supported Diesel Engines," in *Flow and Combustion in Reciprocating Engines*, (Berlin: Springer-Verlag, 2008), doi:10.1007/978-3-540-68901-0_4.
9. Dolak, J.G., Shi, Y., and Reitz, R.D., "A Computational Investigation of Stepped-Bowl Piston Geometry for a Light Duty Engine Operating at Low Load," SAE Technical Paper 2010-01-1263, 2010, doi:10.4271/2010-01-1263.
10. Eder, T., Lückert, P., Kemmner, M., and Sass, H., "OM654-Launch of a New Engine Family by Mercedes-Benz," *MTZ Worldwide* 77(3):60-67, 2016.
11. Li, X., Sun, Z., Du, W., and Wei, R., "Research and Development of Double Swirl Combustion System for a DI Diesel Engine," *Combustion Science and Technology* 182(8):1029-1049, 2010, doi:10.1080/00102200903544271.
12. Yoo, D., Kim, D., Jung, W., Kim, N. et al., "Optimization of Diesel Combustion System for Reducing PM to Meet Tier4-Final Emission Regulation without Diesel Particulate Filter," SAE Technical Paper 2013-01-2538, 2013, doi:10.4271/2013-01-2538.
13. Kurtz, E.M. and Styron, J., "An Assessment of Two Piston Bowl Concepts in a Medium-Duty Diesel Engine," *SAE Int. J. Engines* 5(2):344-352, 2012, doi:10.4271/2012-01-0423.
14. Perini, F., Zha, K., Busch, S., and Reitz, R., "Comparison of Linear, Non-Linear and Generalized RNG-Based k-Epsilon Models for Turbulent Diesel Engine Flows," SAE Technical Paper 2017-01-0561, 2017, doi:10.4271/2017-01-0561.
15. Wang, B.-L., Miles, P.C., Reitz, R.D., Han, Z. et al., "Assessment of RNG Turbulence Modeling and the Development of a

Generalized RNG Closure Model," SAE Technical Paper 2011-01-0829, 2011, doi:10.4271/2011-01-0829.

16. ECN Data Search Page, Engine Combustion Network Website, [cited 8/11/2017]; Available from: https://ecn.sandia.gov/ecn-data-search/.
17. Perini, F. and Reitz, R.D., "Improved Atomization, Collision and Sub-Grid Scale Momentum Coupling Models for Transient Vaporizing Engine Sprays," *International Journal of Multiphase Flow* 79:107-123, 2015, doi:10.1016/j.ijmultiphaseflow.2015.10.009.
18. Busch, S., "Light-Duty Diesel Combustion," presented at *the DOE Vehicle Technologies Office and Hydrogen and Fuel Cells Program Annual Merit Review*, Washington, DC, June 6, 2017, available online: https://energy.gov/eere/vehicles/downloads/vehicle-technologies-office-merit-review-2017-light-duty-diesel-combustion.
19. Reitz, R.D. and Bracco, F.B., "On the Dependence of Spray Angle and other Spray Parameters on Nozzle Design and Operating Conditions," SAE Technical Paper 790494, 1979, doi:10.4271/790494.
20. Beale, J.C. and Reitz, R.D., "Modeling Spray Atomization with the Kelvin-Helmholtz/Rayleigh-Taylor Hybrid Model," *Atomization and Sprays* 9(6):623-650, 1999, doi:10.1615/Atomiz Spr.v9.i6.40.
21. Munnannur, A. and Reitz, R.D., "Comprehensive Collision Model for Multidimensional Engine Spray Computations," *Atomization and Sprays* 19(7):597-619, 2009, doi:10.1615/AtomizSpr.v19.i7.10.
22. Torres, D.J., O'Rourke, P.J., and Amsden, A.A., "A Discrete Multicomponent Fuel Model," *Atomization and Sprays* 13(2&3):42, 2003, doi:10.1615/AtomizSpr.v13.i23.10.
23. Engine Combustion Network Website, "Small-Bore Diesel Engine," [cited 8/11/2017]; Available from: https://ecn.sandia.gov/engines/engine-facilities/small-bore-diesel-engine/.
24. Perini, F., Zha, K., Busch, S., Miles, P. et al., "Principal Component Analysis and Study of Port-Induced Swirl Structures in a Light-Duty Optical Diesel Engine," SAE Technical Paper 2015-01-1696, 2015, doi:10.4271/2015-01-1696.
25. Xu, H., "Some Critical Technical Issues on the Steady Flow Testing of Cylinder Heads," SAE Technical Paper 2001-01-1308, 2001, doi:10.4271/2001-01-1308.
26. Perini, F., Zha, K., Busch, S., Kurtz, E. et al., "Piston Geometry Effects in a Light-Duty, Swirl-Supported Diesel Engine: Flow Structure Characterization," *International Journal of Engine Research*, 2017, doi:10.1177/1468087417742572.
27. Busch, S. and Miles, P.C., "Parametric Study of Injection Rates with Solenoid Injectors in an Injection Quantity and Rate Measuring Device," *Journal of Engineering for Gas Turbines and Power* 137(10):101503-101503, 2015, doi:10.1115/1.4030095.
28. Sahoo, D., Miles, P.C., Trost, J., and Leipertz, A., "The Impact of Fuel Mass, Injection Pressure, Ambient Temperature, and Swirl Ratio on the Mixture Preparation of a Pilot Injection," *SAE Int. J. Engines* 6(3):1716-1730, doi:10.4271/2013-24-0061.
29. Su, W., Lin, R., Xie, H., and Shi, S.-x., "Enhancement of Near Wall Mixing of an Impinging Jet by Means of a Bump on the Wall," SAE Technical Paper 971616, 1997, doi:10.4271/971616.
30. Su, W., Lin, T.J., Zhao, H., and Pei, Y.Q., "Research and Development of an Advanced Combustion System for the Direct Injection Diesel Engine," *Proceedings of the Institution of Mechanical Engineers Part D-Journal of Automobile Engineering* 219:241-252, 2005, doi:10.1243/095440705X6604.
31. Ebara, T., Amagai, K., and Arai, M., "Penetration Model of a Diesel Spray along a Wall," presented at *the Fourth International Symposium COMODIA*, Kyoto, Japan, July 20-23, 1998.
32. Cornwell, R. and Conicella, F., "Direct Injection Diesel Engines," Patent Number: US 8, 770,168 B2, July 8, 2014.
33. Iikubo, S., Nakajima, H., Adachi, Y. and Shimokawa, K., "Combustion Chamber Structure for Direct Injection Diesel Engine," Patent Number: US 8,156,927 B2, April 17, 2012.
34. Naber, J.D. and Siebers, D.L., "Effects of Gas Density and Vaporization on Penetration and Dispersion of Diesel Sprays," SAE Technical Paper 960034, 1996, doi:10.4271/960034.
35. Arai, M., Amagai, K., and Ebara, T., "Attitude Control of a Diesel Spray under the Coanda Effect," SAE Technical Paper 941923, 1994, doi:10.4271/941923.
36. Zha, K., Busch, S., Miles, P.C., Wijeyakulasuriya, S. et al., "Characterization of Flow Asymmetry during the Compression Stroke Using Swirl-Plane PIV in a Light-Duty Optical Diesel Engine with the Re-Entrant Piston Bowl Geometry," *SAE Int. J. Engines* 8(4):1837-1855, 2015, doi:10.4271/2015-01-1699.
37. Perini, F., Ra, Y., Hiraoka, K., Nomura, K. et al., "An Efficient Level-Set Flame Propagation Model for Hybrid Unstructured Grids Using the G-Equation," *SAE Int. J. Engines* 9(3):1409-1424, 2016, doi:10.4271/2016-01-0582.

Contact Information

Stephen Busch
sbusch@sandia.gov

Acknowledgements

Sandia National Laboratories is a multimission laboratory managed and operated by National Technology and Engineering Solutions of Sandia, LLC., a wholly owned subsidiary of Honeywell International, Inc., for the U.S. Department of Energy's National Nuclear Security Administration under contract DE-NA-0003525. The views expressed in the article do not necessarily represent the views of the U.S. Department of Energy or the United States Government.

The authors thank Sayan Biswas and Chuck Mueller for their help in reviewing the manuscript.

Definitions/Abbreviations

CAD, °CA - Crank angle degrees

CFD - Computational fluid dynamics

(A)SOI$_{main}$ - (After) the start of main injection

(A)TDC - (After) top dead center (firing)

H,T - Helical and tangential intake ports

Nomenclature

A_f - Areas of individual triangulation faces in a horizontal cutting plane

A_{nozzle} - Total cross-sectional area of all injector holes

C_d - Nozzle discharge coefficient

C_μ - Constant in turbulence viscosity equation

$\hat{i}, \hat{j}, \hat{k}$ - Cartesian unit normal vectors

k - Turbulence kinetic energy

$\dot{m}_{inj}$ - Mass rate of injection through all injector holes

$\hat{n}$ - Surface unit normal vector

$\bar{p}_{inj}$ - Average momentum flow rate through a control surface

$\dot{p}_z$ - Vertical momentum flow rate through a control surface

p_z^* - Dimensionless vertical momentum flow rate through a control surface

p - Pressure

r - Radius (measured from cylinder axis)

$\hat{r}$ - Radial unit vector

R_s - Swirl ratio

t - Time

t_{EOIm} - Time of the end of main injection

t_{SOIm} - Time of start of main injection

$\vec{u}$ - Gas velocity vector

u_r, u_θ, u_z - Radial, tangential, and vertical velocity components (derived from Cartesian velocity components)

u, v, w u_1, u_2, u_3 - x, y-, and z-components of mean velocity

u_x, u_y, u_z - Partial derivatives of u with respect to x, y, z

v_x, v_y, v_z - Partial derivatives of v with respect to x, y, z

w_x, w_y, w_z - Partial derivatives of w with respect to x, y, z

u_1', u_2', u_3' - Fluctuating components of velocity

u_{ij} - Second partial derivative of u with respect to i and j

v_{ij} - Second partial derivative of v with respect to i and j

w_{ij} - Second partial derivative of w with respect to i and j

v_{inj} - Injection velocity

$\vec{v}_p$ - Piston velocity

x, y, z x_1, x_2, x_3 - Cartesian coordinates

δ_{ij} - Kronecker delta

ϵ - Dissipation rate of turbulence kinetic energy

θ - Azimuthal angle in cylindrical coordinate system

μ - Molecular (dynamic) viscosity

μ_t - Turbulence viscosity

ρ - Density

τ_{ij} - Reynolds stress

$\dot{\varphi}_z$ - Vertical momentum flux through a control surface

χ_{O_2} - Oxygen volume fraction

χ_{fuel} - Fuel volume fraction

Appendix A: Equations Used to Evaluate the Radial Momentum Equation

CFD Simulation Outputs

The following terms are available, or directly computed, from the simulation output for each node and at each time step:

- Spatial coordinates: x, y, z
- Mean velocity components: $\vec{u} = u_1\hat{i} + u_2\hat{j} + u_3\hat{k}$; in this case the velocity components u_1, u_2, u_3 are used interchangeably with u, v, w
- Gradients of velocity components, for example: $\frac{\partial v}{\partial x} \stackrel{\text{def}}{=} v_x$, $\frac{\partial u_i}{\partial z} \stackrel{\text{def}}{=} u_{i,z}$, etc.
- Second partial derivatives of velocity components, for example: $\frac{\partial^2 w}{\partial x \partial y} \stackrel{\text{def}}{=} w_{xy}$, $\frac{\partial^2 u_i}{\partial y \partial z} \stackrel{\text{def}}{=} u_{i,yz}$, etc.
- Pressure gradients: $\nabla p = \frac{\partial p}{\partial x}\hat{i} + \frac{\partial p}{\partial y}\hat{j} + \frac{\partial p}{\partial z}\hat{k}$
- The molecular viscosity μ
- The turbulent viscosity μ_t and the three components of its gradient: $\frac{\partial \mu_t}{\partial x_i} = \mu_{t,i}$
- The density ρ

Evaluating the Radial Momentum Equation

The Reynolds-Averaged Navier-Stokes radial momentum equation assuming constant density and molecular viscosity is evaluated as:

$$\frac{\partial u_r}{\partial t} = \frac{-1}{\rho}\frac{\partial p}{\partial r} - \left(u_r \frac{\partial u_r}{\partial r} + \frac{u_\theta}{r}\frac{\partial u_r}{\partial \theta} + u_z \frac{\partial u_r}{\partial z} - \frac{u_\theta^2}{r} \right) + \mu \left(\frac{\partial}{\partial r}\left\{ \frac{1}{r}\frac{\partial}{\partial r}\left(r u_r\right) \right\} + \frac{1}{r^2}\frac{\partial^2 u_r}{\partial \theta^2} + \frac{\partial^2 u_r}{\partial z^2} - \frac{2}{r^2}\frac{\partial u_\theta}{\partial \theta} \right) + \frac{1}{\rho}\frac{\partial \tau_{ij}}{\partial r}$$

Each of the terms on the right-hand side must be evaluated using CFD simulation output data, which are given in Cartesian coordinates.

The conversion from Cartesian to cylindrical coordinates is computed as follows:

- $r = \sqrt{x^2 + y^2}$
- $\hat{r} = cos\theta\hat{i} + sin\theta\hat{j} = \frac{x\hat{i} + y\hat{j}}{r}$
- $tan\theta = \frac{y}{x}$
- $z = z$
- $x = rcos\theta; \frac{\partial x}{\partial \theta} = -rsin\theta; \frac{\partial x}{\partial r} = cos\theta$
- $y = rsin\theta; \frac{\partial y}{\partial \theta} = rcos\theta; \frac{\partial y}{\partial r} = sin\theta$
- $u_r = ucos\theta + vsin\theta = \frac{xu}{r} + \frac{yv}{r} = \frac{xu + yv}{\sqrt{x^2 + y^2}}$
- $u_\theta = -usin\theta + vcos\theta$

For $f(x, y, z) \rightarrow F(r, \theta, z)$, the following identity applies:

$$\boxed{\frac{\partial F}{\partial \theta} = \frac{\partial f}{\partial x}\frac{\partial x}{\partial \theta} + \frac{\partial f}{\partial y}\frac{\partial y}{\partial \theta} = -rsin\theta\frac{\partial f}{\partial x} + rcos\theta\frac{\partial f}{\partial y} = -y\frac{\partial f}{\partial x} + x\frac{\partial f}{\partial y}}$$

Radial Pressure Gradient The mean radial pressure gradient is defined as the dot product of the pressure gradient vector and $\hat{r}$:

$$\boxed{\frac{\partial p}{\partial r} = \nabla p \cdot \hat{r} = \frac{\partial p}{\partial x}cos\theta + \frac{\partial p}{\partial y}sin\theta}$$

Convective Terms

$$\frac{\partial u_r}{\partial r} = \frac{\partial}{\partial r}\left(ucos\theta + vsin\theta\right) = \frac{\partial u}{\partial r}cos\theta + \frac{\partial v}{\partial r}sin\theta$$

Applying the chain rule, $\frac{\partial u_r}{\partial r} = \left(\frac{\partial u}{\partial x}\frac{\partial x}{\partial r} + \frac{\partial u}{\partial y}\frac{\partial y}{\partial r} + \frac{\partial u}{\partial z}\frac{\partial z}{\partial r} \right)cos\theta + \left(\frac{\partial v}{\partial x}\frac{\partial x}{\partial r} + \frac{\partial v}{\partial y}\frac{\partial y}{\partial r} + \frac{\partial v}{\partial z}\frac{\partial z}{\partial r} \right)sin\theta$

By definition, $\frac{\partial z}{\partial r} = 0$

So $\boxed{\frac{\partial u_r}{\partial r} = \left(u_x cos\theta + u_y sin\theta\right)cos\theta + \left(v_x cos\theta + v_y sin\theta\right)sin\theta}$

$$\frac{\partial u_r}{\partial \theta} = \frac{\partial}{\partial \theta}\left(\frac{xu + yv}{\sqrt{x^2 + y^2}} \right) = -y\frac{\partial}{\partial x}\left(\frac{xu + yv}{\sqrt{x^2 + y^2}} \right) + x\frac{\partial}{\partial y}\left(\frac{xu + yv}{\sqrt{x^2 + y^2}} \right)$$

This is evaluated using the quotient rule and the chain rule, and simplifies to:

$$\frac{\partial u_r}{\partial \theta} = -\frac{y}{r}\left(xu_x + yv_x + u\right) + \frac{x}{r}\left(xu_y + yv_y + v\right)$$

$$\boxed{\frac{\partial u_r}{\partial \theta} = -sin\theta\left(xu_x + yv_x + u\right) + cos\theta\left(xu_y + yv_y + v\right)}$$

$$\frac{\partial u_r}{\partial z} = \frac{\partial}{\partial z}\left(ucos\theta + vsin\theta\right)$$

θ is independent of z, so $\boxed{\frac{\partial u_r}{\partial z} = u_z cos\theta + v_z sin\theta}$

Viscous Terms

$$\frac{1}{r}\frac{\partial}{\partial r}\left(ru_r\right) = \frac{u_r}{r} + \frac{\partial u_r}{\partial r}$$

$$\frac{\partial}{\partial r}\left\{\frac{1}{r}\frac{\partial}{\partial r}\left(ru_r\right)\right\} = \frac{\partial}{\partial r}\left(\frac{u_r}{r} + \frac{\partial u_r}{\partial r}\right), \text{so}$$

$$\frac{\partial}{\partial r}\left(\frac{u_r}{r} + \frac{\partial u_r}{\partial r}\right) = \frac{r\dfrac{\partial u_r}{\partial r} - u_r}{r^2} + \frac{\partial}{\partial r}\left(\left(u_x cos\theta + u_y sin\theta\right)cos\theta + \left(v_x cos\theta + v_y sin\theta\right)sin\theta\right)$$

This simplifies to

$$\boxed{\frac{\partial}{\partial r}\left\{\frac{1}{r}\frac{\partial}{\partial r}\left(ru_r\right)\right\} = \frac{1}{r}\frac{\partial u_r}{\partial r} - \frac{u_r}{r^2} + \left(u_{xx}cos^2\theta + 2u_{xy}sin\theta cos\theta + u_{yy}sin^2\theta\right)cos\theta + \left(v_{xx}cos^2\theta + 2v_{xy}sin\theta cos\theta + v_{yy}sin^2\theta\right)sin\theta}$$

$$\frac{\partial^2 u_r}{\partial \theta^2} = \frac{\partial}{\partial \theta}\left(\frac{\partial u_r}{\partial \theta}\right) = \frac{\partial}{\partial \theta}\left(-sin\theta\left(xu_x + yv_x + u\right) + cos\theta\left(xu_y + yv_y + v\right)\right)$$

Using the identity $\frac{\partial F}{\partial \theta} = -y\frac{\partial f}{\partial x} + x\frac{\partial f}{\partial y}$ (see above), this reduces to:

$$\boxed{\begin{aligned}\frac{\partial^2 u_r}{\partial \theta^2} = &-sin\theta\left[-y\left(2u_x + xu_{xx} + yv_{xx}\right) + x\left(xu_{xy} + v_x + yv_{xy} + u_y\right)\right] - cos\theta\left(xu_x + yv_x + u\right) + \\ &cos\theta\left[-y\left(u_y + xu_{xy} + yv_{xy} + v_x\right) + x\left(xu_{yy} + 2v_y + yv_{yy} + u_y\right)\right] - sin\theta\left(xu_y + yv_y + v\right)\end{aligned}}$$

$$\frac{\partial^2 u_r}{\partial z^2} = \frac{\partial}{\partial z}\left(\frac{\partial u}{\partial z}cos\theta + \frac{\partial v}{\partial z}sin\theta\right)$$

$$\boxed{\frac{\partial^2 u_r}{\partial z^2} = u_{zz}cos\theta + v_{zz}sin\theta}$$

$$\frac{\partial u_\theta}{\partial \theta} = \frac{\partial}{\partial \theta}\left(-usin\theta + vcos\theta\right)$$

$$\boxed{\frac{\partial u_\theta}{\partial \theta} = \left(yu_x - xu_y\right)sin\theta - ucos\theta + \left(-yv_x + xv_y\right)cos\theta - vsin\theta}$$

Reynolds Stress Term The Reynolds-Averaged Navier-Stokes equations in Cartesian coordinates are expressed using Einstein notation as:

$\frac{\partial u_i}{\partial t} = -\frac{1}{\rho}\frac{\partial p}{\partial x_i} + \frac{\mu}{\rho}\frac{\partial^2 u_i}{\partial x_j \partial x_j} - \overline{u}_j\frac{\partial u_i}{\partial x_j} + \frac{1}{\rho}\frac{\partial \tau_{ij}}{\partial x_j}$, where *i* is a free index corresponding to the 1-, 2-, or 3-direction (x, y, or z in this case); and *j* is a repeated index that represents a summation over *j* values of 1, 2, and 3 (x, y, and z)

The Reynolds stress, $\tau_{ij} = -\rho\overline{u_i'u_j'}$, is modeled using the Boussinesq approximation: $-\rho\overline{u_i'u_j'} = \mu_t\left(\frac{\partial u_i}{\partial x_j} + \frac{\partial u_j}{\partial x_i} - \frac{2}{3}\frac{\partial u_k}{\partial x_k}\delta_{ij}\right) - \frac{2}{3}\rho k\delta_{ij}$. The turbulence viscosity μ_t is defined as $\mu_t = \rho C_\mu \frac{k^2}{\epsilon}$.

- δ_{ij} is the Kronecker delta, defined as $\delta_{ij} = \begin{cases} 0; i \neq j \\ 1; i = j \end{cases}$
- $C_\mu = 0.0845$ as described in [14].
- k is the turbulence kinetic energy and is available as a simulation output; $k = \frac{1}{2}\overline{u_i'u_i'}$
- u_i' are the fluctuating velocity components defined by the Reynolds decomposition
- ϵ is the dissipation rate of turbulence kinetic energy, defined as $\epsilon = \nu\overline{\frac{\partial u_i'}{\partial x_k}\frac{\partial u_i'}{\partial x_k}}$.

The term $\frac{\partial}{\partial x_j}\left(-\rho\overline{u_i'u_j'}\right)$ represents a force vector per unit volume, and is therefore expressed as:

$$\frac{\partial}{\partial x_j}\left(-\rho\overline{u_i'u_j'}\right) = \mu_t\left(\frac{\partial^2 u_i}{\partial x_j \partial x_j} + \frac{\partial^2 u_j}{\partial x_i \partial x_j} - \frac{2}{3}\frac{\partial}{\partial x_j}\left(\frac{\partial u_k}{\partial x_k}\delta_{ij}\right)\right) + \mu_t\left(\frac{\partial u_i}{\partial x_j}\frac{\partial \mu_t}{\partial x_j} + \frac{\partial u_j}{\partial x_i}\frac{\partial \mu_t}{\partial x_j} - \frac{2}{3}\frac{\partial u_k}{\partial x_k}\delta_{ij}\frac{\partial \mu_t}{\partial x_j}\right) - \frac{2}{3}\frac{\partial}{\partial x_j}(\rho k)$$

This results in three components corresponding to the three values of the free index i:

$$\frac{\partial}{\partial x_j}\left(-\rho\overline{u_i'u_j'}\right) = \mu_t\left(u_{i,xx} + u_{i,yy} + u_{i,zz} + u_{1,ix} + u_{2,iy} + u_{3,iz} - \frac{2}{3}\left(u_{1,xi} + u_{2,yi} + u_{3,zi}\right)\right)$$

$$+\left(u_{i,x}\mu_{t,x} + u_{i,y}\mu_{t,y} + u_{i,z}\mu_{t,z} + u_{1,i}\mu_{t,x} + u_{2,i}\mu_{t,y} + u_{3,i}\mu_{t,z} - \frac{2}{3}\left(\mu_{t,i}\left(u_{1,x} + u_{2,y} + u_{3,z}\right)\right)\right) - \frac{2}{3}\frac{\partial}{\partial x_i}(\rho k)$$

The gradient of the product ρk is computed using the same numerical scheme used throughout the CFD simulations. The radial projection of the force due to the Reynolds stress gradient is computed via the dot product with the radial unit vector (defined above):

$$\boxed{\frac{\partial \tau_{ij}}{\partial r} = \frac{\partial}{\partial x_j}\left(-\rho\overline{u_i'u_j'}\right)\cdot\hat{r}}$$

ISSN 0148-7191